WO_3/SnO_2-Modified Graphite Felts as Novel Carbon-Based Positive Electrodes for Zinc-Cerium Redox-Flow Battery (RFB)

by

Omar K. Bin Gah

A thesis

presented to the University of Waterloo

in fulfillment of the

thesis requirement for the degree of

Master of Applied Science

in

Chemical Engineering

Waterloo, Ontario, Canada, 2021

Author's Declaration

I hereby declare that I am the sole author of this thesis. This is a true copy of the thesis, including any required final revisions, as accepted by my examiners.

I understand that my thesis may be made electronically available to the public.

Abstract

Redox flow batteries (RFBs) are promising large-scale energy storage devices that are potentially cost-effective, easily scaled up in size, safe and versatile. RFBs use the chemical reactions of redox species which are dissolved in liquid electrolytes to store electrical energy when demand is low and deliver it during periods of high demand for electricity. Among various RFBs, zinc–cerium redox flow batteries (Zn-Ce RFBs) have received attention as an attractive energy storage system due to their higher open-circuit voltage (OCV) than any other aqueous-based system that has been proposed. However, the performance of Zn-Ce RFB must be enhanced if it is to be successfully commercialized. The electrode structure plays a significant role in the performance of RFBs. Ideal electrodes should perform efficiently under the severe acidic and oxidizing conditions with satisfactory durability. Taking into account the highly acidic and oxidizing conditions on the cerium half-cell, an electrode employed in that side should maintain outstanding electrochemical behavior toward the Ce(III)/Ce(IV) reaction.

Precious metals such as platinum and gold have shown promising performance. However, due to their high cost, the need for cheaper, but effective, electrode materials have become very crucial. Economical carbon-based materials have been shown to provide good kinetic activity for the Ce(III)/Ce(IV) reaction. Particularly, polyacrylonitrile (PAN)-based graphite felt (GF) exhibits excellent chemical and electrochemical catalytic activity due to its excellent stability and conductivity, high specific surface area and enhanced three-dimensional structure. This study concentrated on examining the utilization of modified graphite felts (GFs) as a positive electrode for the Zn-Ce RFB system. Solvothermal method was used to introduce metal oxides electrocatalysts on the GF surface. Tungsten

trioxide (WO_3) and tin dioxide (SnO_2) served as promising metal oxides to enhance hydrophilicity and electrochemical activity of GF. A binary mixture of WO_3 and SnO_2 was used as a novel candidate to improve the electrochemical activity of pristine GFs for the Ce(III)/Ce(IV) reaction.

Half-cell electrochemical characterization was performed using cyclic voltammetry (CV) at room temperature in a 0.05 M Ce(III) MSA + 1.0 M MSA electrolyte. The ratio of the cathodic peak current density to the anodic peak current density (I_{pc}/I_{pa}), peak potential separation (ΔE_p) and coulombic charge obtained from the CVs were used to assess the activity and reversibility of the Ce(III)/Ce(IV) reaction on the various GF electrode samples. The durability of the modified GF electrodes was evaluated by subjecting them to multiple CV cycles over the voltage range from 0.56 to 1.8 V vs. Ag|AgCl at a scan rate of 10 mV s^{-1}. Modified GFs with the novel binary metal oxide containing both WO_3 and SnO_2 exhibited superior stability and electrocatalytic performance toward the Ce(III)/Ce(IV) reaction compared to unmodified GF and those modified with the individual oxides alone. Among all GF samples, the binary WO_3-SnO_2 modified GF showed the highest values of anodic charge (Q_a), cathodic charge (Q_c) and Q_c/Q_a. Q_c/Q_a of as-received GF was found to improve from 17.8% to 50.1% when modified with 0.05M W and 0.05M Sn. The microstructure and composition of the modified GFs were analyzed by scanning electron microscopy (SEM), energy dispersive X-ray spectroscopy (EDX) and X-ray photoelectron spectroscopy (XPS). Overall, findings obtained from these analyses confirmed the successful decoration of W and Sn on the GFs.

Acknowledgements

Firstly, I would like to thank my supervisor Professor Mark Pritzker for giving me the chance to work on this exciting project and also for his continued help, support and guidance throughout my graduate studies. Without his guidance, this work would never have been achieved.

Great thanks to Dr. Jeff Gostick, Dr. Michael Pope, Kiana Amini and any other faculty and staff in the department for their kind help during my graduate study. Also, I would like to thank Hadhramout Foundation for its funding and support.

Finally, special thanks to my family, including my mother, father, wife and my young princess "Joury" for their love and support.

Dedication

This is dedicated to the one I love.

Table of Contents

List of Figures

List of Tables

Chapter 1

INTRODUCTION

The increase in worldwide energy demand is attributed to the development of the global economy and population growth [1, 2]. Moreover, the emergence of the modern lifestyle and dependence on electronic devices and automobiles have significantly contributed to the increase in the global energy demand. The global population has increased at a fast rate of 1.14% per year whereas the total global energy demand has risen fast at rate of 1.52% per year [3]. Since 1971, energy demand which depends mainly on fossil fuels has doubled [2]. The demand for electricity which is the most common form of energy consumed (40% of all energy used in United Sates in 2012 was electricity) is anticipated to double by 2025 [4]. Along with this large demand, global CO_2 emissions must be lowered to combat climate change [1]. Currently, fossil fuels account for approximately 70% of global CO_2 emissions [5]. This has led countries to seek alternative energy sources that are clean, sustainable and low-priced. These include renewable solar, wind, hydroelectric, geothermal, tidal, and biofuel sources that already have a variety of applications [2].

Renewable energy (RE) has received immense interest due to its remarkable environmental benefits and is predicted to offer a solution to the world demand for secure and sustainable energy [5]. As a result, many countries have invested in improving the efficiency of renewable energy and developing its applications [1]. Nuclear energy has also been considered to be clean, efficient, with low emission rates to the environment. Yet, many countries are not interested in the nuclear energy because of its severe side effects and its high capital and operating costs [5]. While more than 4% of electricity is currently provided by wind and solar energy, this supply is expected to increase to above 25% by 2030 [6]. Despite all the advantages related to renewable energy usage, major challenges still remain, including the intermittent availability of solar energy and wind sources, and energy storage problems [7].

Energy storage technologies (ESTs) have received attention recently because of their promise to provide energy to consumers all the time [7]. They can be integrated with renewable energy sources to store excess energy during low demand and deliver it at peak demand periods. Additionally, ESTs help to save electricity for distributors and consumers who are required to follow policies of hourly pricing [6]. The three main categories of electrical energy storage technologies are flywheels and supercapacitors, geological storage technologies and energy storage devices. Supercapacitors and flywheels are described as high-power, low-energy storage applications [1, 7]. They have not been widely used due to their higher material costs. However, they are appropriate for short-term storage and power management. Geological storage technologies are high-energy and high-power large-scale systems, but are limited to specific geographical locations for installation, costly construction and maintenance and can cause potential devastation of biological systems.

Pumped hydroelectric storage (PHS) and compressed air energy storage are the most common examples of geological storage. Currently, PHS is by far the most widely used, accounting for $\backsim 99.2\%$ of total worldwide storage capacity [6]. Battery storage technologies are expected to offer an optimum solution for client demand such as power delivery and irregular power generation from renewable energy sources. At present, the lead-acid battery is the most popular battery storage. Although it has low investment costs, it has limited charge/discharge capacity and requires continual maintenance and replacement. Lithium-ion, nickel-cadmium, nickel and sodium-based batteries are other examples that can operate over large number of cycles at higher current densities, but are expensive to install and operate [1, 7]. In terms of large-scale energy storage, reduction–oxidation (redox) flow batteries (RFBs) are promising cost-effective energy candidates with superior design, scale-capacity, safety and versatility [8, 9].

In general, RFB uses the chemical reactions of redox species which are dissolved in liquid electrolytes to store electrical energy. RFB can store the energy generated from renewable sources when demand is low and deliver it during periods of high demand for electricity [10]. In this way, RFB is able to achieve what is called diurnal peak shaving or load leveling [11].

Peak load shaving is a process of storing energy when the electricity demand is low and utilizing it during peak demand periods. It flattens the load curves at the times of peak energy demand by using the stored energy at the times of lower demand. As shown in Figure 1.1, Uddin et al demonstrated how energy consumption varies during each day [12]. It can be seen that the peak demand occurs at a midday and in the evening whereas it reaches its lowest level during the night.

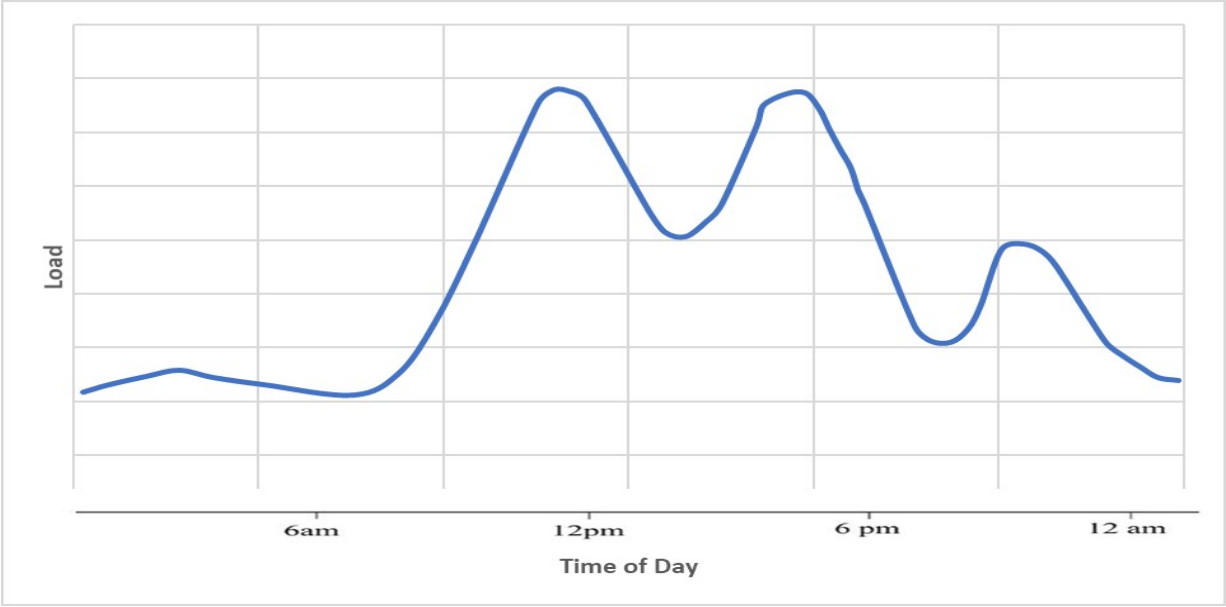

Figure 1.1: Electric production during the day [12]

Peak shaving can be achieved by integrating ESTs into the electrical grid. ESTs can be charged using electricity from the grid at off-peak periods; this stored energy can be released during peak-demand periods, as it is illustrated in Figure 1.2. Battery energy storage systems (BESS), including RFBs, are attractive devices for peak shaving over mid-term durations less than 5 hr [12]. RFBs are particularly cost-effective for peak shaving and energy storage in large-scale systems. Additionally, RFBs can avoid the need for over-designing the electrical grid since its capacity is based on peak demand requirements, not average demand requirements. This leads to excess production of electricity during low demand periods. This excess energy would provide the electricity available from the grid to charge RFBs during low demand periods.

RFBs can also supply uninterrupted power and combine both heat and electrical power

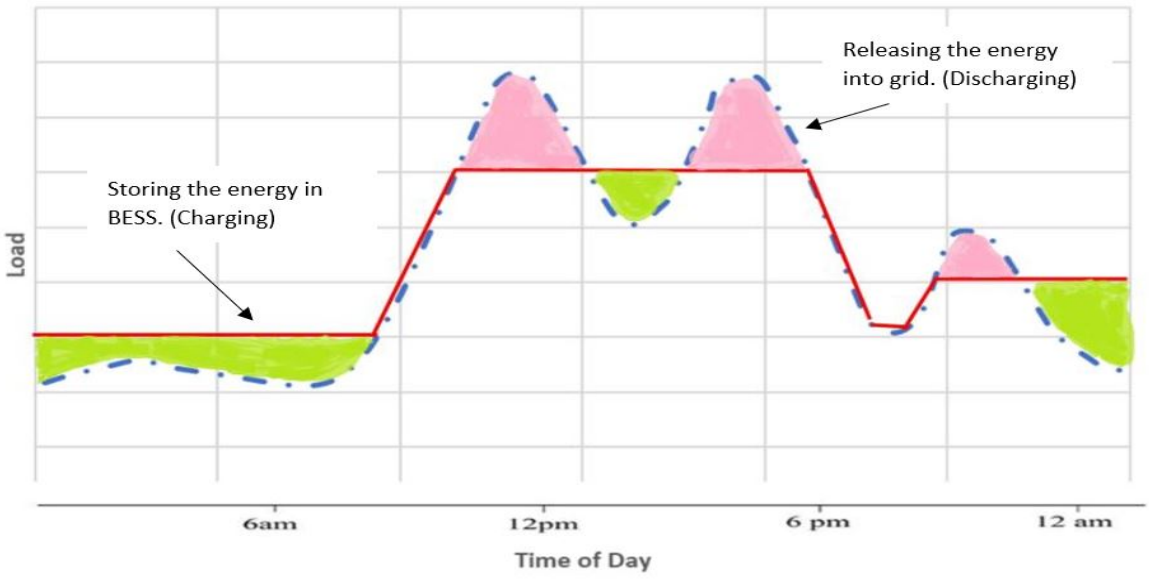

Figure 1.2: Peak shaving using ESTs [12]

systems. RFB has a number of advantages over other electrochemical storage systems. For instance, the storage of the electroactive materials in reservoirs outside the cell where the redox reactions occur effectively decouples the power and energy capacities of the battery, which greatly facilitates scale-up, design and operation. Additionally, optimal energy efficiencies of RFBs have been obtained by operation at higher temperatures and adjusting electrolyte flowrate [6, 10, 11].

Obviously, electrodes are important components of any battery. The positive and negative electrodes in RFBs play vital roles in providing active sites for the redox reactions and enhancing both their reversibility and kinetics [8, 9]. For the most part, an optimal electrode should meet the following specifications [13]:

1. large, specific surface area

2. superior electrocatalytic activity
3. excellent electronic conductivity
4. wide potential window
5. impressive chemical stability and durability, especially in strongly acidic or basic media
6. low price

Whereas the electrodes that have been studied to date meet some of these requirements, challenges remain with identifying materials that simultaneously meet all of these specifications.

1.1 Thesis Objectives

Zinc–cerium redox flow batteries (Zn-Ce RFBs) have received considerable attention as an attractive energy storage system due to its higher open-circuit voltage (OCV) than any other aqueous-based system that has been proposed. The OCV of Zn-Ce RFB is ca. 2.46V at full charge while the OCV of the all-vanadium battery is only 1.26 V [10]. This results in higher energy density and power output which can be achieved at a given current density [14]. In this system, methanesulfonic acid (MSA) has served as the favorable electrolyte for both the positive Ce(III)/Ce(IV) and negative Zn/Zn(II) half-cells [15]. Despite the aforementioned advantages, some problems must be overcome. A critical problem associated with the negative electrode during charge is the hydrogen evolution

reaction (HER), arising from the very low potential of the negative electrode, which can lead to premature battery failure [10, 16]. Another problem during charge occurs at the positive electrode where the highly oxidizing conditions lead to the onset of the oxygen evolution reaction (OER).

The broad aim of this project is to work toward the development of cost-effective Zn-Ce-RFB with improved power density and durability. Specifically, this research focuses on enhancing the electrochemical performance of the positive electrode of Zn-Ce RFBs. An experimental investigations were conducted to explore the use of carbon-based materials as potential substitutes for costly platinum-based materials. A key focus of this study on the use of metal oxides as a promising catalyst for the Ce(III)/Ce(IV) reaction. In particular, the use of tungsten trioxide (WO_3) and tin dioxide (SnO_2) are examined under various conditions as low-cost and efficient nanocatalysts to enhance the electrochemical activity of graphite felt electrodes for use in Zn-Ce RFBs.

1.2 Thesis Outline

The thesis is composed of six chapters, including this introductory chapter. Chapter 2 discusses the scientific background of the research, and provides fundamental information regarding redox flow batteries as an energy storage application. It also introduces zinc-cerium (Zn-Ce) chemistry as the basis for a promising RFB that has received significant interest in recent years. Chapter 3 is devoted to an overview of the use of carbon-based materials as non-precious electrodes for RFB systems. In addition, it discusses the various electrode modification methods used in this study. Chapter 4 describes the materials

and equipment used in this research. Moreover, it presents the experimental procedures involved in investigating electrode efficiency. The 5^{th} chapter presents the experimental findings of the project, with particular focus on the different conditions used to modify the graphite felt substrate employed as the positive electrode in a Zn-Ce RFB. The final chapter summarizes the main findings and proposes recommendations for future work on carbon-based materials as the positive electrode in Zn-Ce RFBs.

Chapter 2

REDOX FLOW BATTERY

2.1 Introduction

A redox flow battery (RFB) is a secondary battery exploiting reversible electrochemical reactions in liquid electrolytes to convert electrical energy to chemical energy and vice versa [13]. Additionally, an RFB is a flow-based device that serves to store and release energy through charge and discharge processes, respectively [1, 16]. In contrast to conventional static batteries, the energy is stored in flowing electrolytes rather than the electrodes, which allows the RFB to operate for a longer life with less maintenance than a conventional battery [17, 9]. Hence, RFBs are usually known as regenerative fuel cells where electricity is generated from the conversion of energy stored in incoming fuels containing two soluble redox couples. The electroactive substances, which are dissolved in the liquid electrolytes, are stored in two separate external tanks. The liquid electrolytes are then pumped through the two half-cell compartments usually separated by an ion exchange

membrane that blocks the mixing of the electrolytes. The structure of the redox flow battery is illustrated schematically in Figure 2.1.

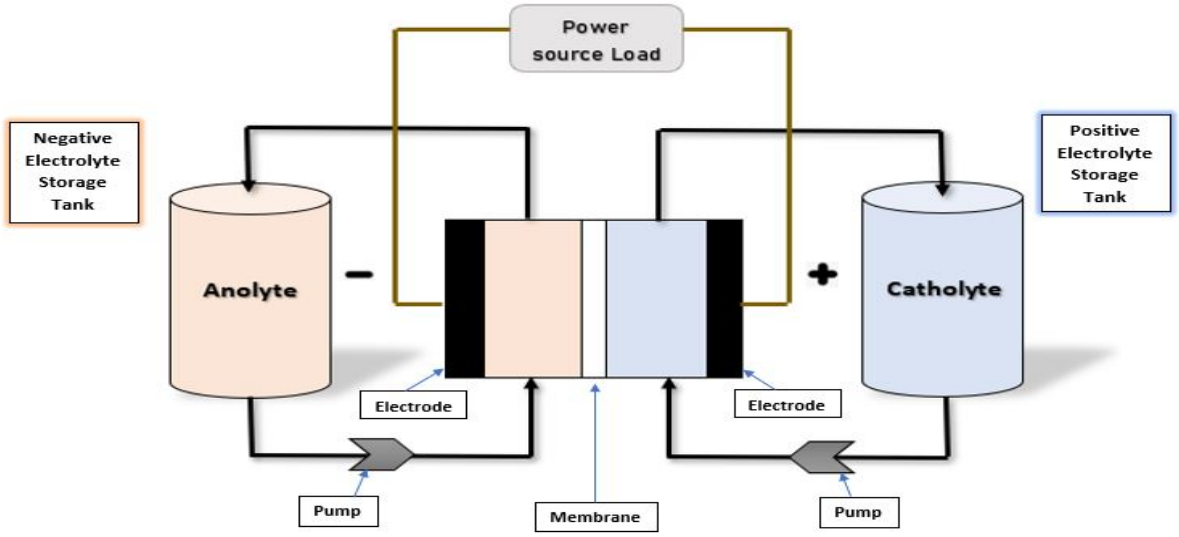

Figure 2.1: Schematic diagram of a redox flow battery

Typically, a RFB unit cell is composed of two compartments where the redox reactions occur. In addition to the two electrodes, current collectors and ion exchange membranes are also involved in the RFB cell. Negative and positive electrolytes flow through the negative and positive compartments, respectively, and serve as energy carriers [16, 6, 7, 13]. The number and the active surface area of electrodes in each unit cell affect the output power delivered by RFB systems, while the volume of the external storage tanks and the electrolyte concentration determine the energy density [1, 11, 9]. Consequently, RFBs have a fundamental advantage over other electrochemical storage systems in that power and energy storage can be optimized independently [6].

Multiple stacks of cells can be also used for RFB systems. Cell stacks are composed of bipolar electrodes connected either in series or parallel (Figure 2.2) [18]. Bipolar plate serves as a current collector and mechanical support for the stack while enhancing current flow between multiple cells in the cell stack [19, 20, 21, 22]. Such a bipolar design increases the power density generated by an RFB by enabling more electrodes to be used in a stack and reducing ohmic losses.

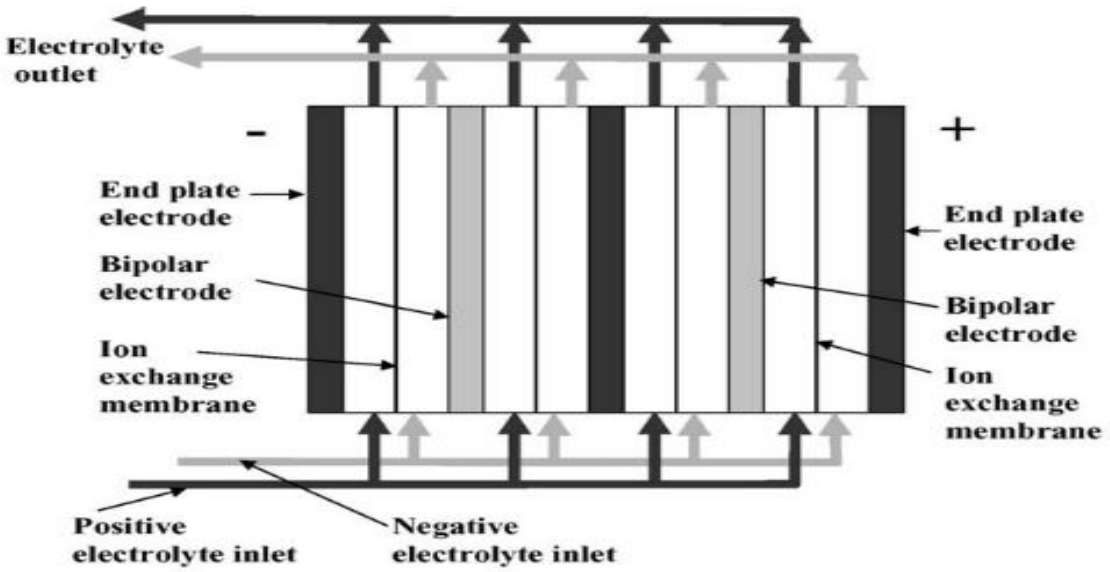

Figure 2.2: Bipolar-electrode stack of four cells [18]

The battery performance is generally evaluated in terms of three efficiencies: coulombic efficiency (CE), voltage (VE) and energy (EE). CE is determined from the ratio of the number of coulombs passed during discharge to that during charge, while VE is obtained from the ratio of the discharge cell voltage to the charge cell voltage. EE is the product of CE and VE [23].

2.2 History of Redox Flow Batteries

The first RFB based on zinc-chlorine chemistry was invented in the 19th century by the French scientist Charles Renard [1]. Subsequently, Kangro proposed in 1949 the concept of employing the same element having different oxidation states on the two sides of the battery [7]. The first device based on this idea was an all-chromium RFB that made use of the Cr(III)/Cr(II) redox reaction at the negative electrode and the Cr(IV)/Cr(III) reaction at the positive electrode. In the 1970s, the US National Aeronautic and Aerospace Administration (NASA) led the expansion of modern RFB technology during the first oil crisis. This research concentrated on the development of iron-chromium (Fe-Cr) redox flow battery. Electrolytes containing redox species Fe(II)/Fe(III) and Cr(II)/Cr(III) were dissolved in hydrochloric acid-based electrolytes on the positive and negative sides, respectively [6, 4]. However, problems related to the crossover of electroactive substances, undesirable hydrogen evolution, and poor reversibility of the Cr(II)/Cr(III) reaction have limited the commercialization of this Fe-Cr RFB [13, 1].

All-vanadium redox-flow batteries (VRFBs) were first introduced in 1988 by Skyllas-Kazacos *et al.* [7]. Vanadium is an attractive basis for an RFB since it can exist in several oxidation states. Using sulfuric acid-based electrolytes for both compartments, Skyllas-Kazacos *et al.* employed V(IV)/V(V) and V(II)/V(III) redox reactions on the positive and negative side, respectively [16]. The widespread expansion of VRFBs compared to Fe-Cr RFB has been ascribed to the higher cell potential and less of a problem associated with crossover. Furthermore, less hydrogen evolution occurs at the negative electrode because of the higher potential of the V(II)/V(III) redox reaction. As a consequence, VRFB has received a great deal of interest to serve as a large-scale energy storage technology.

Despite the aforementioned advantages of VRFBs, several challenges with their use still remain. For instance, the limited solubility of the various vanadium species in the electrolytes results in poor energy density. Additionally, ion exchange membranes that have excellent chemical stability, ion selectivity and ionic conductivity are needed [13, 22]. Ultimately, a number of studies have been conducted to improve vanadium ion solubility and lower major costs of the VRFB system [16, 24, 19, 25].

2.3 Types of Redox Flow Batteries

Based on the nature of the electroactive species, RFBs can be divided into three main categories:

- dual liquid where the two redox couples store their chemical energy entirely in electrolytes, such as all-vanadium RFBs
- dual solid where the two redox couples store their chemical energy entirely on the two electrode surfaces such as lead-lead dioxide RFBs
- hybrid where one redox couple stores its chemical energy in its electrolyte and the other redox couple stores its chemical energy on its electrode surface, such as zinc-cerium, zinc-bromine and zinc-chlorine RFBs

This study will be limited to investigate a hybrid flow battery, specifically the zinc-cerium system. In this type of battery, solid deposition/stripping (i.e., Zn/Zn(II)) occurs on the negative electrode, while a redox reaction (Ce(III)/Ce(IV)) involving only soluble

species occurs on the positive electrode. In this type of RFB, operating variables such as the thickness and structural morphology of deposited metal determine the energy storage capacity. In the next section, background on zinc-cerium RFBs will be provided in more details.

2.4 Zinc-Cerium RFB

The innovation of a novel zinc-cerium hybrid redox flow battery (Zn-Ce RFB) was first introduced by Electrochemical Design Associates Inc. in the 1990s [14, 11]. The U.S. patent by Clarke in 2004 suggested the use of methanesulfonic (MSA) acid as an ideal electrolyte for the zinc-cerium battery [16, 26]. This was followed by research at Plurion Ltd., the University of Southampton, and University of Strathclyde that contributed significantly to the advancement of this technology [9, 14]. Due to the large differences of the standard electrode potentials of the two redox couples in aqueous media, the zinc-cerium system exhibits a higher open-circuit voltage (OCV) than any other aqueous-based system that has been proposed. The OCV of Zn-Ce RFB is *ca.* 2.46V at full charge while the OCV of the all-vanadium battery is only 1.26 V [14]. Consequently, the electric power provided at a given current density is relatively high. Table 2.1 [27] presents the half-cell reactions and their OCV for various redox flow systems. Using carbon felts as positive electrodes, the Zn-Ce system was capable to operate at 50 mA cm^{-2} with high charge (coulombic) and voltage efficiencies of >92% and >68% , respectively [28]. Zn-Ce RFBs have several advantages such as low cost, low toxicity and abundant supply of the electroactive species on both sides [29].

Ce(IV) and Zn(II) exhibit high solubilities of 8.0 x 10^{-1} mol L^{-1} and 2.0 mol L^{-1}, respectively, in MSA. The solubility of the cerium salts (i.e., cerium (III) carbonate) is ~10 times higher in MSA than sulfuric acid. In comparison to hydrochloric acid, MSA exhibits excellent conductivity and stability, while maintaining lower toxicological risk (LD_{50} =1000 mg kg^{-1}) as well [14, 30, 28].

Table 2.1: Electrochemical reactions and system OCV for various redox flow cells [27]

Cathodic redox reactions	Anodic redox reactions	Cell OCV (V)
$Fe^{3+} + e^- \rightleftarrows Fe^{2+}$	$Cr^{2+} \rightleftarrows Cr^{3+} + e^-$	1.19
$VO_2^+ + 2H^+ + e^- \rightleftarrows VO^{2+} + H_2O$	$V^{2+} \rightleftarrows V^{3+} + e^-$	1.26
$PbO_2 + 4H^+ + SO_4^- + 2e^- \rightleftarrows PbSO_4 + 2H_2O$	$Cu \rightleftarrows Cu^{2+} + 2e^-$	1.35
$ClBr_2^{2-} + e^- \rightleftarrows 2Br^- + Cl^-$	$VBr_2 + Br^- \rightleftarrows VBr_3 + e^-$	1.35
$Br_2 + 2e^- \rightleftarrows 2Br^-$or $Br_3^- + 2e^- \rightleftarrows 3Br^-$	$2\ S_2^{2-} \rightleftarrows S_4^{2-} + 2e^-$	1.36
$VO_2^+ + 2H^+ + e^- \rightleftarrows VO^{2+} + H_2O$	$Zn \rightleftarrows Zn^{2+} + 2e^-$	1.76
$O_2 + 4H^+ + 4e^- \rightleftarrows 2H_2O$	$V^{2+} \rightleftarrows V^{3+} + e^-$	1.49
$Br_2 + 2e^- \rightleftarrows 2Br^-$or $Br_3^- + 2e^- \rightleftarrows 3Br^-$	$Zn \rightleftarrows Zn^{2+} + 2e^-$	1.82
$PbO_2 + 4H^+ + 2e^- \rightleftarrows Pb^{2+} + 2H_2O$	$Pb \rightleftarrows Pb^{2+} + 2e^-$	1.69
$Ce^{4+} + e^- \rightleftarrows Ce^{3+}$	$Zn \rightleftarrows Zn^{2+} + 2e^-$	2.46

One disadvantage of a large OCV is that it makes it easier for secondary reactions to take place at both electrodes. In Zn-Ce RFBs, undesired hydrogen and oxygen evolution side reactions occur at the negative and positive electrodes, respectively, during charge. The equilibrium potential of the Ce(III)/Ce(IV) reaction falls in the range between 1.28 and 1.72V *vs.* SHE depending on the electrolyte. Using MSA as electrolyte, the primary

half-cell reactions are:

Positive electrode:

$$2\mathrm{Ce}\left(\mathrm{CH_3SO_3}\right)_3 + 2\mathrm{CH_3SO_3H} \underset{Discharge}{\overset{Charge}{\rightleftharpoons}} 2\mathrm{Ce}\left(\mathrm{CH_3SO_3}\right)_4 + 2\mathrm{H^+} + 2\mathrm{e^-} \tag{2.1}$$

($\mathrm{E^0}$ = 1.44 V *vs.* SHE)

Negative electrode:

$$\mathrm{Zn}\left(\mathrm{CH_3SO_3}\right)_2 \quad + 2\mathrm{H^+} + 2\mathrm{e^-} \underset{Discharge}{\overset{Charge}{\rightleftharpoons}} \mathrm{Zn} + 2\mathrm{CH_3SO_3H} \tag{2.2}$$

($\mathrm{E^0}$ = -0.76 V *vs.* SHE)

The secondary undesired reactions during charge are:

Oxygen evolution reaction (OER) at the positive electrode, i.e.,

$$2\mathrm{H_2O} \underset{Discharge}{\overset{Charge}{\rightleftharpoons}} \mathrm{O_2} + 4\mathrm{H^+} + 4\mathrm{e^-} \tag{2.3}$$

($\mathrm{E^0}$ = 1.23 V *vs.* SHE)

hydrogen evolution reaction (HER) at the negative electrode, i.e.,

$$2\mathrm{H^+} + 2\mathrm{e^-} \underset{Discharge}{\overset{Charge}{\rightleftharpoons}} \mathrm{H_2} \tag{2.4}$$

($\mathrm{E^0}$ = 0 V *vs.* SHE)

The standard emf of the Zn-Ce system based on a standard electrode potential of 2.4 V *vs* SHE for reaction 2.1 is:

$$2\mathrm{Ce}\left(\mathrm{CH_3SO_3}\right)_3 + \mathrm{Zn}\left(\mathrm{CH_3SO_3H}\right)_2 \underset{Discharge}{\overset{Charge}{\rightleftharpoons}} \mathrm{Zn} + 2\mathrm{Ce}\left(\mathrm{CH_3SO_3}\right)_4 \tag{2.5}$$

(E^0 = 2.4 V *vs.* SHE)

Protons permeate across the membrane from the positive compartment to the negative compartment during charge to maintain electroneutrality on each side [14]. Figure 2.3 depicts the main electrochemical processes taking place inside the battery [31].

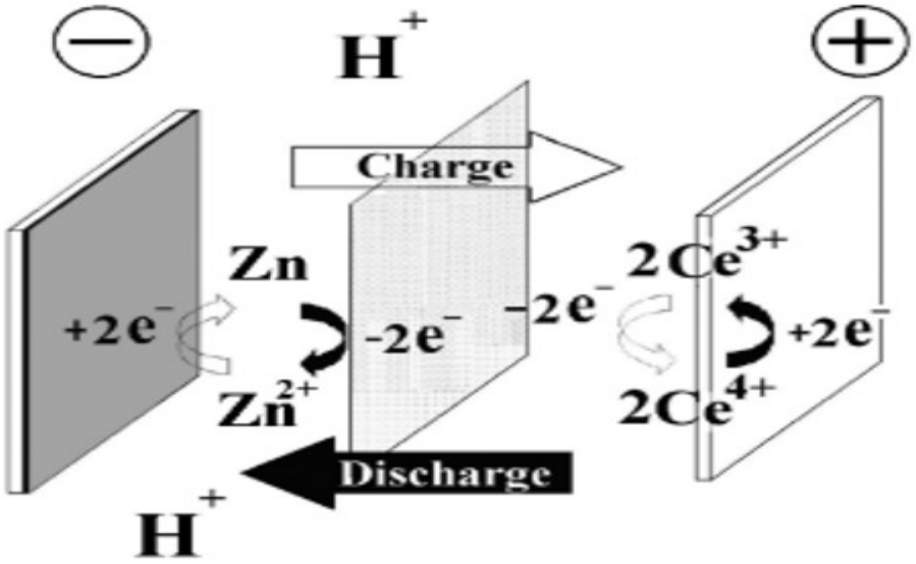

Figure 2.3: Hybrid zinc-cerium RFB [31]

Although zn-ce RFB has high charge/discharge rates with superior energy power compared to other flow batteries, some problems must be overcome. A critical problem associated with the negative electrode during charge is the HER, the undesirable self-discharge and dissolution of the deposited zinc in electrolyte and the very low potential of the negative electrode, which can lead to premature failures and internal short circuits [10, 16]. Another problem during charge occurs at the positive electrode where the highly oxidizing

conditions lead to the onset of the OER. Hence, a good understanding of the electrochemical kinetics of Ce(III)/Ce(IV) couple in MSA under different conditions is vital [32, 9, 33].

In the two subsections that follow, more details concerning the major operating variables that influence the electrochemical performance on the negative and positive side of Zn-Ce RFBs are presented. In addition, challenges associated with each compartment will be discussed.

2.4.1 Negative Compartment

The electrodeposition and dissolution of zinc take place at the negative electrode of a Zn-Ce RFB, as mentioned previously. This redox couple has a very negative standard electrode potential of -0.76 V *vs.* SHE in acidic solution [16]. Furthermore, the Zn/Zn(II) reaction exhibits excellent kinetics with minimal overpotential during discharge and charge. For these reasons, the Zn(II)/Zn couple has been viewed as an attractive negative electrode reactions in a number of aqueous-based RFBs. Not surprisingly, the formation of a thick, uniform zinc layer is desirable in all zinc-based RFBs. However, the quality of zinc deposits has been a problem in zinc-halogen batteries due to a number of factors. Cell design, charge conditions, electrolyte type and electrode substrate are the most important factors affecting the quality of zinc layers formed on inert substrates [14].

Another phenomenon associated with zinc that is critical to RFB performance is its spontaneous self-discharge. The self-discharge rate occurs due to the high tendency of electrodeposited Zn to oxidize in an acid electrolyte. Thus, hydrogen evolution is enhanced because of the increased corrosion rate of zinc electrodeposit in the electrolyte [31]. Furthermore, hydrogen evolution reaction and dendritic growth are other challenging

problems that occur during zinc electrodeposition. The hydrogen evolution reaction always take places before any zinc deposition since the standard potential of Zn(II)/Zn reaction is more negative than that of H^+/H_2 (see equations 2.2 and 2.4). Dendrites are defects that can lead to internal short-circuit and mechanical damage of the membrane [34].

For these reasons, numerous studies have been carried out to enhance zinc deposition, optimize the geometry of the electrolyte flow channels and mitigate both the HER secondary reaction and the deterioration of zinc layers [35]. Electrolyte composition and hydrodynamics play a significant role in the structure of zinc electrodeposits. Efforts to modify the electrolyte composition have been among the most effective approaches to improve the quality of zinc deposits and extend the battery cycle life. Selection of the appropriate electrolyte can lead to an improvement in the kinetics of the Zn/Zn(II) reaction and optimize the electrodeposition process. For example, MSA has been reported to inhibit the formation of dendrites during zinc deposition at concentrations higher than 2.0 mol L^{-1} [36]. Furthermore, MSA is less corrosive and volatile than sulfuric acid and more environmentally friendly compared to other acids employed in RFBs [35, 28].

Previous investigations have shown that the deposit morphology on an electrode is affected by electrolyte flowrate [34, 16, 35]. Together, these studies have shown that a higher electrolyte flowrate promotes a more uniform deposit and reduces the thickness of the Nernst diffusion layer. Dendritic growth was shown to be significantly diminished when the linear electrolyte velocity was raised to 2 cm s^{-1} compared to that observed in a static electrolyte.

In addition to the aforementioned strategies, the use of electrolyte additives has also been shown to enhance the Zn/Zn(II) reaction by inhibiting the HER. Organic additives are

widely used in industry for zinc deposition. For example, classical glue has been employed in sulfuric acid electrolytes to decrease the zinc grain size while gum Arabic has been used to modify 2-dimentional orientation of the zinc deposit [34, 37]. Nonylphenoloxyethylene, 2-butyne-1,4-diol, 1-butyl-3-methylimidazoliumion and perfluorinated additives have been shown to suppress the HER and improve the current efficiency of zinc electrodeposition [16]. In addition, the presence of inorganic additives can lead to significant improvement in the coulombic and voltage efficiencies of zinc deposition during operation of Zn-Ce RFBs. Indium (III) and lead(II) are examples of soluble additives that can inhibit the HER [38].

Recent studies have pointed out that the use of alternative electrolytes can aid the negative zinc reactions for zinc-cerium RFB. A recent study by Amini and Pritzker [10, 15] proposed the addition of chloride ions to methanesulfonate solution in a strongly acidic media of Zn-Ce RFBs. The mixed-methanesulfonate-chloride electrolyte has notably facilitated the zinc redox reaction, and optimized the deposited zinc-layer during cathodic polarization. The improved results were attributed to the formation of bridges between the substrate and zinc ions leading to promote the electron transfer via the adsorption of chloride ions on the electrode surface.

Collectively, work is needed to further promote zinc deposition over the HER and ensure dendrite-free deposition by optimizing the design of electrolyte channels used in RFB cell.

2.4.2 Positive Compartment

The Ce(III)/Ce(IV) reaction exhibits superior kinetics over the V(IV)/V(V) reaction at comparable concentration [39]. Indeed, cerium is found abundantly in nature and is a relatively inexpensive material. In contrast to vanadium and bromium, cerium exhibits

lower toxicity and risk to the environment [40]. Due to an empty 4f-shell, cerium acquires the most stable tetravalent oxidation state in solution among all rare-earth ions. However, in acidic environment, Ce(IV) ion is a strong one-electron oxidizing agent and its oxidizing power can be compared to that of Mg(III) salts and Pb(IV) oxides [41]. The Ce(IV)/Ce(III) redox couple is involved in several industrial processes, including gas scrubbing, mediated electrosynthesis, decontamination and cleaning, and energy storage [42]. In the case of energy storage, redox flow battery provides an excellent illustration in which the very positive standard potential of Ce(III)/Ce(IV) is exploited to achieve a high energy density. In particular, Ce(III)/Ce(IV) has served as the positive electrode reaction in numerous flow batteries such as zinc-cerium (Zn-Ce), vanadium-cerium (V-Ce), half fuel cell of hydrogen gas-cerium (H_2-Ce) [32]. In the following paragraphs, the use of the Ce(III)/Ce(IV) reaction in the Zn-Ce RFB and opportunities for further improvement will be discussed.

The kinetics of the Ce(III)/Ce(IV) couple depends very strongly upon the nature and concentration of the electrolyte. Indeed, the electrolyte serves as the energy carrier for the electroactive species. Gschneidner *et al.* reported that the electrical potential of this redox couple rises with an increase in the perchloric acid concentration, but decreases if the concentrations of both nitric and sulfuric acid rise [41]. This can be attributed to the formation of stable perchlorate complexes in the presence of Ce(III) ions whereas Ce(IV) ions tend to be more inactive than Ce(III). Due to the reduction of NO_3^- and the oxidation of Cl^-that can occur during battery operation, the use of nitric acid and hydrochloric acid, respectively, as supporting media is limited. Additionally, cerium salts suffer from relatively poor solubility in sulfuric acid solutions, leading to the precipitation of $H_2Ce(OH)_2\,(SO_4)_2$ solid at lower concentrations [43, 44]. Likewise, perchloric acid is not

used in electrochemical applications due to its highly oxidizing and explosive nature [42]. Therefore, the need for a very stable alternative electrolyte in which Ce(III) and Ce(IV) have high solubility to facilitate the Ce(III)/Ce(IV) reaction is crucial.

Much of the previous literature on supporting electrolytes for zn-ce RFBs has focused particular attention on the use of MSA as a desirable acidic media. Indeed, the solubility of Ce(III) in MSA has been shown to exceed 8.0×10^{-1} mol L^{-1}. This solubility of cerium (III) carbonate salts is tenfold greater than in H_2SO_4 [14, 35, 16]. Compared to HCl, MSA exhibits a comparable conductivity and stability with low vapour pressure and minimal risk of corrosion [28, 42]. Generally, a high concentration of 4 M MSA is required to maintain high Ce(III) solubility and suppress oxygen evolution reaction (OER), but this also raises the viscosity of the electrolyte [28, 34]. Thus, it is important that the electrolyte not become too viscous since this has a deleterious effect on mass transfer and degrades RFB performance. However, the use of a lower concentrations of 2-3 M MSA reduces the solubility of Ce(IV) in the solution.

Several studies have been conducted to evaluate the optimal electrolyte composition and temperature. As shown in Figure 2.4, the effect of MSA concentration on the Ce(III) solubility is opposite to that on the Ce(IV) solubility at room temperature [42]. The Ce(III) solubility is high at low MSA concentration and decreases quite sharply as the acid concentration is raised, whereas elevated MSA concentrations are necessary for a satisfactory Ce(IV) solubility. Consequently, an intermediate MSA concentration of $\sim$4 mol L^{-1} is required in order that the solubilities of both Ce(III) and Ce(IV) exceed 1.0 mol L^{-1}. Leung *et al.* investigated the reversibility of Ce(IV)/Ce(III) couples in MSA using a platinum disk electrode at various electrolyte concentrations and temperatures [32]. Both

the rate of oxidation of Ce(III) and reduction of Ce(IV) were observed to increase with temperature up to a maximum at 49.8 °C. Furthermore, the Ce(III)/Ce(IV) reaction in MSA was found to be quasi-reversible and diffusion-controlled. Based on this study, Leung *et al.* proposed that a positive electrolyte of 0.8 mol L^{-1} cerium (III) methanesulfonate in 4.0 mol L^{-1} MSA at 70 °C is optimum for RFB system [32]. Another study found that the reversibility of the Ce(IV)/Ce(III) is significantly advanced at temperatures in the range of 40-60 °C [35].

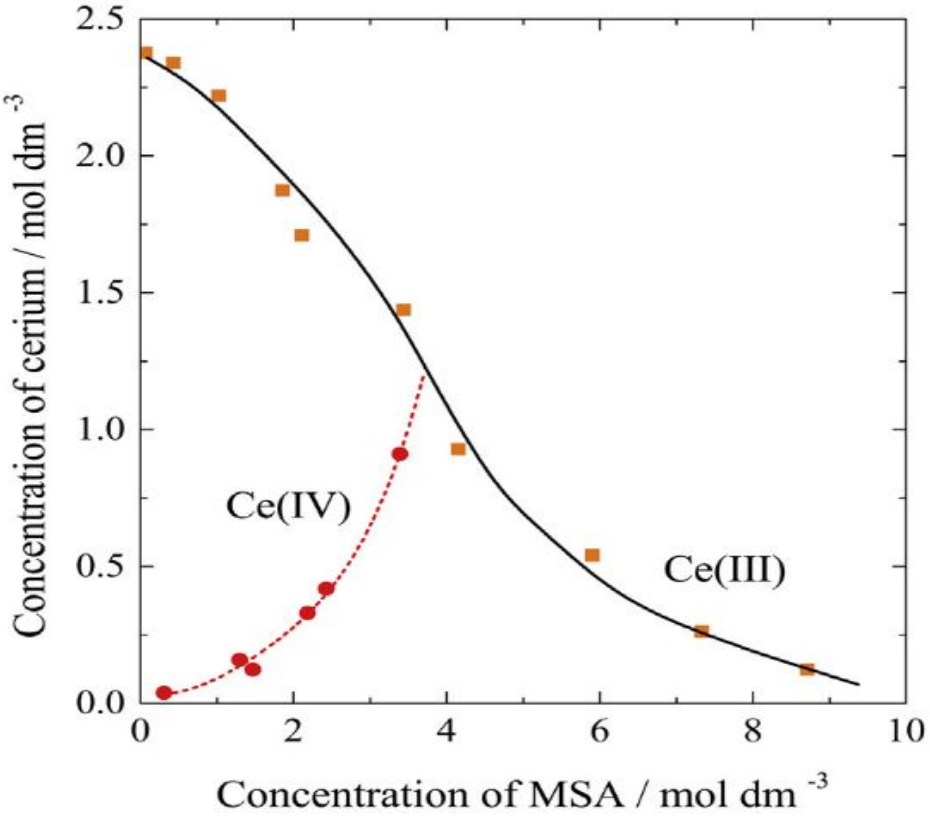

Figure 2.4: The solubility of cerium active species in methanesulfonic acid (MSA) at room temperature [42]

A large and growing body of literature has recently focused on enhancing electrolyte stability and facilitating redox reactions at high Ce concentrations and lower acid compositions. For example, the use of mixed acid media has been shown to be one of the most effective approaches for enhancing the performance on the positive side of Zn-Ce RFBs. Xie *et al.* examined the reversibility of Ce(III)/Ce(IV) reaction on platinum electrode in mixed-acid supporting electrolyte containing MSA and sulfuric acid [26, 44]. They found that the separation between the anodic and cathodic CV peaks in mixed acid (1 mol L^{-1} MSA + 1 mol L^{-1} H_2SO_4) decreased to 103 mV compared to 462 mV and 141 mV in single acid electrolytes containing 3 mol L^{-1} MSA and 2 mol L^{-1} H_2SO_4, respectively. Ce(IV) was found to exhibit a higher diffusion coefficient and the Ce(III)/Ce(IV) reaction to have a higher standard rate constant in the mixed acid, indicating that its use is also beneficial for mass transfer and electrode kinetics. In addition, the solubility of cerous sulfate ($Ce_2(SO_4)_3$) determined on the basis of the saturation ion product $\left(K_{sip} = \left[Ce^{3+}\right]^2 \left(\left[SO_4^{2-}\right] + \left[HSO_4^-\right]\right)^3\right)$ is significantly improved in mixed acid (K_{sip} = 5.97) compared to that obtained in sulfuric acid alone (K_{sip} = 0.86). This improved solubility in mixed acid has a positive effect on cerous salt stability. For instance, a solution containing 1 mol cerium sulfate dissolved in mixed acid (2 mol L^{-1} MSA + 0.5 mol L^{-1} H_2SO_4) exhibited exceptional stability at 40 °C for more than 1 month. Nikiforidis carried out cyclic voltammogram experiments on a Pt disk electrode at 25 °C in an electrolyte involving 0.6 mol L^{-1} dissolved cerium [45]. Nikiforidis showed the addition of smaller amount of hydrochloric acid (0.5 - 1 mol L^{-1}) to 4 mol L^{-1} MSA noticeably improved the reversibility and kinetics of the Ce(III)/Ce(IV) reaction due to the formation of complex intermediates [45]. On the other hand, the use of a mixed H_2SO_4-HNO_3 electrolyte did not enhance Ce(III)/Ce(IV) reversibility, which it can be ascribed to the failure of sulfate

and nitrate ions to form complex intermediates [45]. Overall, these studies highlighted the need for further investigation on mixed acids to optimize both the electrolyte stability and redox reversibility of dissolved cerium.

To date, the use of additives in the positive electrolyte was explored in a number of studies. Diethylenetriaminepentaacetate (DTPA), sulfosalicylic acid (SSA), phthalic anhydride, sulfocarbamide, ethylene-diaminetetraacetic acid (EDTA) and silver nitrate are some examples of additives that affect electrolyte stability and Ce(III)/Ce(IV) redox activity [26]. DTPA, sulfosalicylic acid, phthalicanhydride and EDTA have been shown to improve both the Ce(III)/Ce(IV) reversibility and electrolyte stability. In contrast, silver nitrate has been shown to enhance only the redox activity of cerium ions, while sulfocarbamide improves the electrolyte stability without enhancing redox reaction kinetics [26]. Sulfosalicylic and sulfamic acid have also been evaluated as additives for the Ce(III/IV) redox reaction and found to only mildly enhance reaction kinetics [40].

In addition to the use of single acid and mixed acid media with or without additives, mixed electrolytes have also been shown to be promising for the kinetic of the Ce(III)/Ce(IV) reaction. A mixed electrolyte contains more than one electroactive species. Currently, cerium ferrous and cerium nitroso-R-salt (NRS,1-nitroso- 2-naphthol-3,6- disulfonic acid disodium) are mixed electrolytes that have been evaluated for use in Zn-Ce RFBs. For instance, the positive electrolyte in a zinc-cerium/ferrum (Zn-CeFe) redox flow battery contains both Ce (III) and Ce(IV) and Fe(II) and Fe(III). The Zn-CeFe RFB show better charge-discharge performance than Zn-Ce RFB since the Fe(II)/Fe(III) reaction exhibits faster kinetics than Ce(III)/Ce(IV) [26]. Given these promising results, further research is warranted to evaluate the kinetics of various redox reactions that can be combined with

Ce(III)/Ce(IV) on the positive side.

Equally important, the electrode structure contributes significantly to the performance of redox flow batteryies. In essence, ideal electrodes should perform efficiently under the severe acidic and oxidizing conditions with satisfactory durability. The reversibility of Ce(III)/Ce(IV) has been studied on several electrodes including platinum, gold and carbon-based materials [26]. In the early years of RFB development, precious metals were shown to provide the best performance. However, due to their high cost, the need for cheaper, but effective, electrode materials has become very crucial. Economical carbon-based materials have been found to exhibit promising kinetic activity for the Ce(III)/Ce(IV) reactions [15, 34]. Additionally, carbon-based materials do not exhibit oxide layer formation during the oxidation of Ce(III) during charge. An early investigation by Leung *et al.* reported that platinized titanium meshes (3D) and carbon felts were more stable and active for Ce(IV) conversion than two-dimensional electrodes, including reticulated vitreous carbon, carbon polyvinyl-ester and graphite [28]. Interestingly, carbon felt was found to provide striking charge and voltage efficiencies of 92% and 68%, respectively which are much closer to that obtained on platinized titanium electrodes which achieved 99.4% coulombic efficiency and 59.9% voltage efficiency at at a current density of 50 mA cm^{-2} [28]. A similar study by Nikiforidis *et al.* evaluated the effect of temperature on the reversibility of Ce(III)/Ce(IV) in MSA on several electrode materials, including platinum, platinum-iridium-coated and carbon [45]. Among these electrodes, the carbon materials showed the best electrochemical behavior toward Ce(III)/Ce(IV) reversibility, but experienced durability problems under the highly acidic and oxidizing conditions on the positive side [45]. One possible remedy for this degradation is to decorate the carbon-based electrodes with a metal or metal oxide

electrocatalysts [35]. The use of metal and metal oxide electrocatalysts for carbon-based materials will be discussed in the following chapter.

Chapter 3

CARBON-BASED ELECTRODES

In this chapter, the use of carbon-based materials as non-precious metal electrodes for RFB systems will be discussed. Also, the various modification methods used to improve both the durability and electrocatalytic efficiency of porous, three-dimensional electrodes will be explored as well.

3.1 Introduction

Carbonaceous materials are widely used as electrodes for electrochemical applications. Due to their moderate cost, chemical stability in acidic medium and broad working potential window, carbon materials are considered promising electrode materials for RFBs [46, 47]. Additionally, carbon-based electrodes boast interesting attributes due to their thermal stability and high surface area that make them useful for many electrochemical applications [48]. Indeed, numerous carbon-based materials have been employed as electrodes for RFBs.

Among these, carbon felt (CF), graphite felt (GF), carbon paper (CP), carbon plastic, glassy carbon and graphite powder have shown promising electrochemical performance with satisfactory durability in acid media. In particular, polyacrylonitrile (PAN)-based CF and GF have been shown to exhibit superior chemical and electrochemical catalytic activity due to their excellent stability and conductivity, high specific surface areas and enhanced three-dimensional structure [46].

Textile (polyacrylonitrile (PAN)), cellulosic (rayon) and pitch-based precursors are well-known precursors widely used in the production of graphite/carbon felts [49]. The three major steps in the manufacture of PAN-based CF and GF are stabilization, carbonization and graphitization of the precursor, as shown in Figure 3.1 [47]. Carbonization is particularly crucial since it involves configurational changes to the structure.

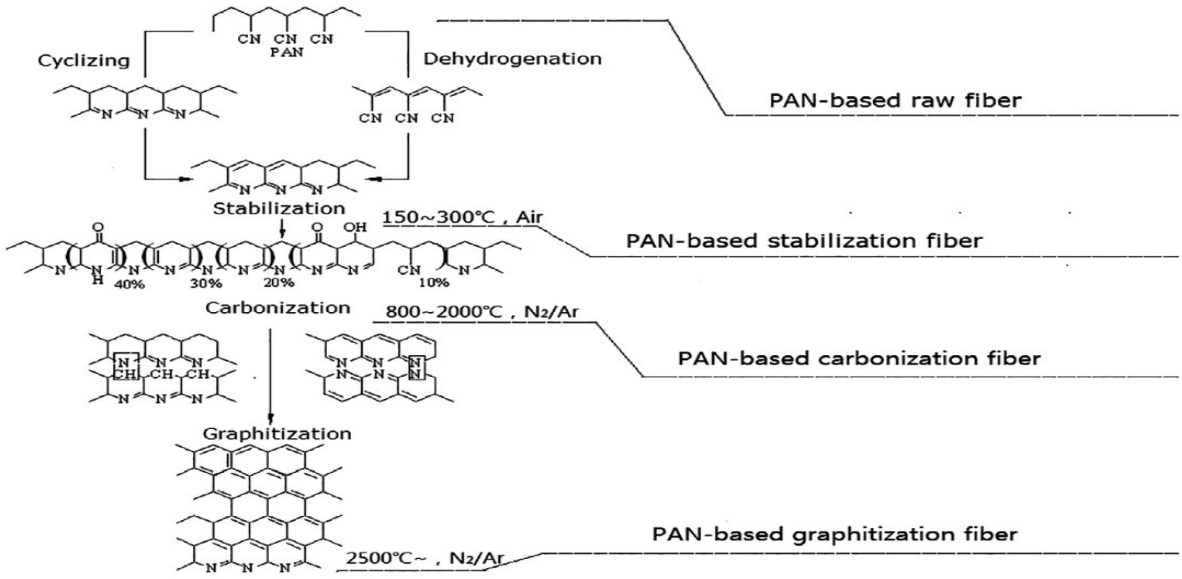

Figure 3.1: Manufacture steps and structural characterization of PAN-based fibers [47]

In the production of carbon fibers, needle-punching is usually carried out prior to graphitization. This helps control the internal and external structure and thickness of manufactured felts. Figure 3.2 shows the needle-punching step in which the barbs on the needles act to hook and pack fibers together vertically. Another layer of fibers is laid on top of the first one and needle-punching is repeated. This not only hooks and packs together the fibers within the second layer, but it also knits the two layers to each other. More layers are added and this process is repeated until a felt of desired thickness is obtained. After needle-punching, the carbon felts are subjected to thermal treatment and graphitized in an inert atmosphere (N_2/Ar) to the temperature ranging from 2000 – 2600 °C to produce graphite felts [49]. In general, the properties of the produced felts rely mostly upon the type of precursors and operating conditions of the manufacturing process.

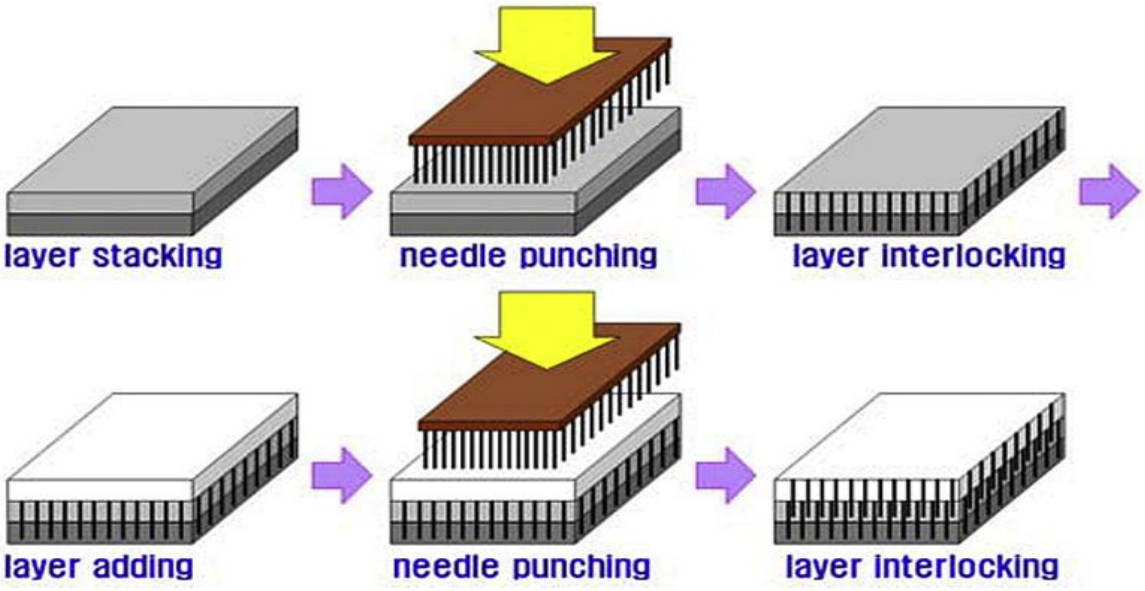

Figure 3.2: Manufacture steps and structural characterization of PAN-based fibers [49]

The present work concentrates on examining the utilization of graphite felts (GFs) as a positive electrode for the Zn-Ce RFB system. Furthermore, the effect of various modification techniques to enhance the hydrophilicity and electrochemical activity of GF electrodes and boost the kinetics of the Ce(III)/Ce(IV) reaction. The following sections provide an overview of the previous research on the use of GF as electrodes for RFB applications. This will cover several methods of surface treatment that are believed to improve the electrocatalytic activity of GF electrodes.

3.2 Graphite Felt (GF)

Graphite is a crystalline structure consisting of sp^2-hybridized carbon atoms assembled as planar hexagonal frames stacked on top of each other [48]. It is an abundant and cost-effective electrode material used for numerous electrochemical and environmental applications. Through a variety of techniques, graphite can be exfoliated to form another material called graphene made up of the single layers of sp^2-hybridized carbon atoms. The stacked layers in graphite are joined together by weak Van der Waals bonds formed by delocalized π-orbital electrons. The dimensions of the hexagonal unit cell of graphite are $a = 2.46$ Å and $c = 6.71$ Å [50]. Graphite fibers packed together as felt has been widely used as the electrode material for RFB systems.

Graphite felt (GF) has a three-dimensional network porous structure with a large surface area. It is also electrochemically stable, corrosion resistant, electrically conductive and relatively inexpensive [51, 52]. Zhong et al. investigated the electrochemical activity of two graphite felts based on polyacrynitrile (PAN) and rayon precursors for the redox

reactions in an all-vanadium redox flow battery [53]. Scanning electron microscopy (SEM) was conducted to characterize the surface microstructure of the two felts. In addition, the surface area, pore size and electrical resistivity were determined. The PAN-based felt exhibited superior electrical conductivity and electrochemical performance over the rayon-based one. In contrast to PAN-based felt, XPS analysis indicated that the rayon-based felt upon thermal treatment reacted spontaneously with oxygen to form higher surface-oxygen concentration of C=O groups [53]. The author concluded that in addition to the oxygen functional groups, several factors such as precursor substance, microstructure, active surface area and hydrophilicity that must be considered to fully understand the major variables leading to enhance the performance of the graphite felt electrodes for VRFB.

Despite its advantages, pristine GF still degrades over time under strong acidic environments, especially when used as an electrode in the positive half-cell of VRFB (V(IV)/V(V)) and ZnCe-RFB (Ce(III)/Ce(V)) in which sulfuric acid and MSA are employed as electrolytes, respectively. Additionally, when graphite felts reach the high temperatures required for graphitization, they become highly hydrophobic, hindering electrolyte accessibility to the GF surface [54]. Therefore, several approaches have been proposed to enhance the electrochemical activity. In most recent studies, this has involved enhancing the active surface area and electrochemical activity of the GF through two major modification methods as demonstrated in Figure 3.3 [55]. Firstly, enhancement of the surface morphology and chemical structure has been carried out by acid and base treatment, thermal treatment and electrochemical oxidation [51, 56, 57]. This introduces oxygen functional groups on the GF surface which are responsible for improving both the electrochemical reversibility of the redox couples involved in RFB systems and the surface wettability [58]. This improvement

is manifested in terms of lower charge transfer resistance (R_{ct}) and faster electrode kinetics [52]. The second method to enhance the electrocatalytic activity is to introduce electrocatalytic species directly on the GF surface. These electrocatalytic species include metals (Cu, Pt, Ir, Pd, Au, Bi, Sb, etc.), metal oxides (ZrO_2, WO_3, Mn_3O_3, SnO_2, CeO_2, $NiCoO_2$, TiO_2, $CeZrO_2$, etc.) and carbon-based nanostructured substances (graphene, nanofibers, carbon nanotubes, carbon nanorods etc.) [9, 56, 57]. This leads to better GF durability and conductivity and low series resistance [52]. As shown in Figure 3.3 each modification method has its limitations. Hence, more research is warranted to improve the effectiveness of each method.

The durability of graphite felts under the severe conditions prevailing during RFB operation has not been widely studied. Therefore, another objective of the current study will be to investigate the durability of graphite felts used as positive electrode for zn-ce RFB and determine the impact of various modification approaches on electrochemical performance and active surface area. The following sections will present the common carbon-based material treatments that have been commonly used for energy storage technology, specifically RFBs.

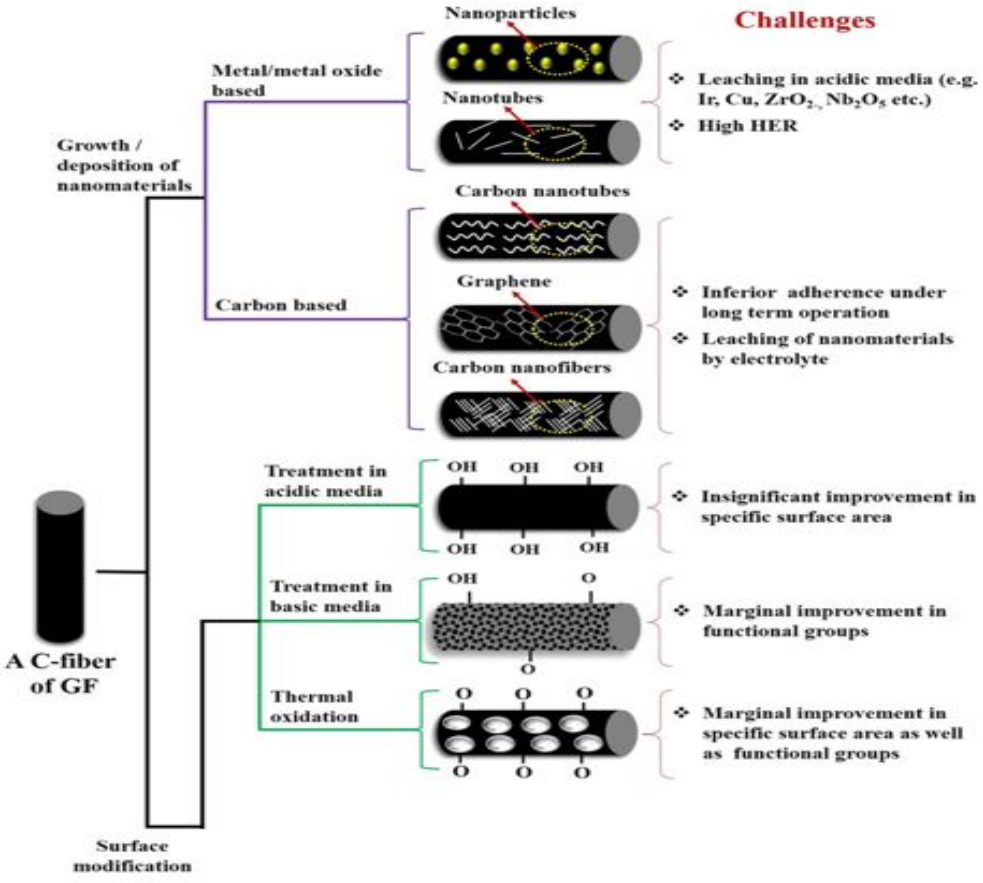

Figure 3.3: Summary of the modification methods used for GF [55]

3.3 Modification of Carbon Materials

3.3.1 Thermal Treatment

Thermal treatment has been widely employed to upgrade the electrochemical performance of electrodes in various redox flow battery systems. This is a long-standing method that was introduced close to 100 years ago [13]. Thermal modification in the presence of oxy-

gen facilitates the formation of oxygen-containing functional groups on the carbon-based surface. This enhances the carbonaceous materials in two different ways: its hydrophilicity and redox activity for redox reactions operating in RFBs [23].

In 1992, Skyllas-Kazacos and co-workers first thermally treated GF in air for use in an all-vanadium RFB [59]. This approach involved thermal activation for different durations at different temperatures. GF modified thermally at 400 °C for 30 h was shown to exhibit a significant upgrade in the electrochemical activity for the V(II)/V(III) and V(IV)/V(V) reactions compared with untreated samples. This enhancement was ascribed to the formation of surface functional C-OH and C=O groups which act as active sites for the redox reaction [59]. Kim *et al.* analyzed the impact of different surface treatments, including thermal modification, on the electrochemical performance of CF electrodes in an all-vanadium RFB [60]. Modification was carried out over the range of 300 to 600 °C for 5 h under air flow. The optimal electrochemical performance using galvanostatic charge–discharge test was obtained for a CF modified at 500 °C. The cell energy efficiency was enhanced significantly from 68 to 75%. Kim *et al.* noted that the thermal treatment also increased the CF surface area in addition to generating surface oxygen-containing functional groups. Ultimately, the improvement in the electrochemical performance of CF was attributed to the introduction of surface functional groups and the increase in defects formed on CF surface [60]. Similarly, thermal treatment under N_2 flow mixed with 1% O_2 in a tubular furnace at 1000 °C for 1 h yielded a remarkable increase in the CF surface area by a factor of 700 [61]. In recent years, many studies on the thermal treatment of carbon-based materials for all-vanadium RFB have been conducted [22, 23, 19, 62]. However, few studies on the impact of thermally modified carbon-based materials on the electrochemical

performance of Zn-Ce RFBs have been reported.

In 2015, Nikiforidis [63] thermally modified porous graphite electrodes for use in the positive compartment of zinc-cerium RFBs. The impact of thermal activation in generating a larger and more electroactive surface area to enhance the Ce(III)/Ce(IV) reaction was investigated. Physical degradation of the graphite structure was observed when it was treated at 600 °C for more than 9.5 h. On the other hand, thermal treatment at 300 °C did not lead to any improvement in Ce(III)/Ce(IV) kinetics. The optimum treatment was found to be at 600 °C for 9 h and yielded enhanced reversibility (quasi-reversibility) and higher reduction/oxidation peak current densities. The optimization of electrochemical activity for the treated graphite electrode was ascribed to the formation of oxygen-containing functional groups on the electrode surface. Nevertheless, more research is needed to explore the effect of other thermal modification conditions on Ce(III)/Ce(IV) reversibility and kinetics.

3.3.2 Chemical Treatment

Chemical treatment involving the use of various oxidants (i.e., $K_2Cr_2O_7$, $(NH_4)_2S_2O_8$ and H_2O_2) and acids (i.e. H_2SO_4 and/or HNO_3), has been studied to enhance the electrochemical performance of carbon-based electrodes [64, 49, 65, 57]. Previous studies have highlighted the positive effect of combining both thermal and chemical treatments to introduce functional phenol (C-O), carboxyl (C=O) and nitrogen-containing groups (-NH_2), on the GF surface [16, 58]. In the absence of modification, GF possesses a hydrophobic surface with limited active sites [51]. Hence, in order for GF to become a good electrocatalyst, thermochemical activation should improve both its wettability and charge-transfer

activity [66].

An early investigation by Sun and Kazacos examined the use of acid treatment with sulfuric acid, nitric acid and mixtures of both to introduce functional groups on the GF surface [59]. Treatment in a hot 98% H_2SO_4 solution for 5 hr yielded a GF electrode with superior electroactivity in all-vanadium RFB. The improvement in electroactivity was attributed to the introduction of oxygen-containing functional groups (C-O and C=O) on the GF surface. On the other hand, treatment of GF with HNO_3 or a combination of H_2SO_4 and HNO_3 did not have any significant effect. To determine the effects of introducing nitrogen- and oxygen-containing functional groups on the GF surface, Flox *et al.* conducted thermal treatment in a NH_3/O_2 (1:1) atmosphere [66]. This study indicated that treatment of GF at 500 °C for 24 h improved the electrochemical activity for the VO_2^+/VO^{2+} redox couple significantly due to the enhancement of electron transfer and electrolyte accessibility on the electrode surface. Surface analysis showed that the oxygen and nitrogen content on the treated GF increased to 32 and 8 % (atomic), respectively. In another major study, Hassan and Tzedakis proposed a novel thermo-chemical surface treatment of GF by exposing it to boiling potassium dichromate solution in 5M (H_2SO_4) [65]. The activated GF served as the positive electrode in an all-vanadium redox flow battery. Surface activation was conducted at various temperatures (100 to 160 °C) for different durations (2 h to 8 h). The optimal electrochemical activity was obtained after treatment at 140 °C for 2 h. Fourier transform infrared spectroscopy and linear sweep voltammetry analysis confirmed the increase of the surface density of carbon-oxygen sites on the GF surface after activation from 5.3 $\times 10^{16}$ to 200 $\times 10^{16}$ (groups/cm^2 of GF) [65].

As noted above, most of the chemical treatment studies to date have been concerned

with the all-vanadium RFB system. Few investigations exploring the effect of chemical activation on GF for cerium-based RFB systems have been reported. Na *et al.* suggested the use of a 1:3 mixture of concentrated sulfuric acid and nitric acid in the case of a cerium-lead RFB system [67, 68]. The acid treatment was carried out at 80 °C for 10 h as a pre-treatment step in order to introduce phenolic (C-O), carboxylic (C=O) groups on the GF surface before exposing it to metal oxide treatment. On the whole, chemical modification shows great promise as a simple and cost-effect approach to activate GF surfaces.

3.3.3 Polymer-Based Treatment

Conducting polymers, including polyaniline (PANI) and polypyrrole (PPy), have been used extensively for electrode enhancement due to their excellent conductivity, good durability and simplicity of synthesis [49]. However, their application so far has been limited since they became electrochemically unstable after 100 charge-discharge cycles due to polymer expansion and degradation [69]. PANI is a well-known polymer employed for energy storage applications. It has attracted the most attention because of its excellent capacitive properties, ease of acid-base doping and cost-effectiveness [70, 71]. PANI can be formed easily on carbon-based surfaces by electrochemical or chemical deposition from a solution containing aniline monomer [49]. Furthermore, PANI can be combined with other materials such as metal oxides and can serve as a catalyst support for metal oxide particles. As a result, a synergistic structure is formed between the metal oxide and conducting polymer which enhances the electrochemical activity of the composite electrode [69]. Researchers have attempted to evaluate the impact of such conducting polymer-metal oxide combina-

tions on the electrochemical performance of various energy storage devices such as Li-ion batteries and supercapacitors.

Kadam *et al.* investigated the catalytic efficiency of a PANI/WO_3 thin film for application in a supercapacitor [71]. In this study, a tungsten oxide film was deposited on a commercial steel substrate via a hydrothermal process conducted at 180 °C for 90 min. Chemical bath deposition was then conducted to form PANI films on WO_3. The specific capacitance degradation of the modified PANI/WO_3 supercapacitor was observed to decline by 2.61% compared to the unmodified supercapacitor due to excellent cyclic stability. Also, the presence of PANI caused the WO_3 to be more finely dispersed so that its surface area increased significantly. In another study, the synthesis of a PANI/WO_3 nanocomposite film on various substrates was carried out using electrodeposition [69]. Geng *et al.* combined the electrodeposition of WO_x and electropolymerization of aniline [72]. The PANi-WO_x composite film was formed on exfoliated graphite for pseudocapacitor materials. This film was able to retain 91.6% of its initial energy capacity after 5000 galvanostatic charge-discharge cycles, while achieving an energy density of 95.8 Wh kg^{-1} at a power density of 650 W kg^{-1}.

Collectively, these studies demonstrate the synergy between WO_3 and conducting polymers for supercapacitors. Yet, a solid understanding of the chemistry involved in their interaction and the improved electrochemical performance of carbon-based electrodes employed in RFBs is still lacking and warrants further inquiry.

3.3.4 Metal and Metal Oxide Treatment

GF exhibits attractive features for use as electrodes in RFBs. It has a porous structure with low cost and excellent stability in acidic media. However, a number of obstacles hinder its scaled-up use. Poor kinetics and limited reversibility of the V(IV)/V(V)and Ce(III)/Ce(IV) reactions are examples of the inherent drawbacks that affect the electrochemical performance of GF electrodes [68, 73, 74]. Hence, decorating metals and metal oxides on the GF surface as electrocatalysts is an effective strategy aimed at enhancing redox reaction kinetics and GF durability.

For the most part, the incorporation of metals and metal oxides on GF surfaces has been carried out mainly to improve the conductive properties of carbon-based electrodes. In contrast with other thermal and chemical methods, modification with metals and metal oxides does not require heating for a longer period or the use of concentrated acid solutions. In particular, these methods involve the deposition/coating from a solution containing metal-based salts, such as WCl_6, $SnCl_4$, $Ce(NO_3)_3$ etc. [9].

Modification with metals is carried out using various methods such as impregnation and electrodeposition where GF is immersed in solutions containing metal ions. The method used and the modification time determine the thickness of the metal deposited on the GF surface [49]. Iridium, ruthenium, platinum, gold and palladium are examples of precious metals incorporated as catalysts on GF surfaces that have improved the reversibility of the $VO^{2+}/VO_2{}^+$ couple reaction [75, 68]. However, several problems such as moderate bifunctional efficiency, catalysis of H_2/O_2 evolution, poor adhesion to the substrate, metal toxicity and high cost have limited their use in RFBs [76, 9, 49]. To address some of these challenges, the introduction of metal oxides on the GF surface has been explored

[73, 52, 77, 78, 75, 79, 80, 81] as an alternative to the use of precious metals for large-scale RFB systems.

Transition metal oxide (TMO) electrocatalysts possess valuable properties that make them desirable for electrochemical applications. These include multiple oxidation states, high chemical stability, eco-friendliness and different chemical structures [76]. Moreover, TMOs are naturally abundant and cheap compared to noble metal catalysts [9, 81]. In spite of the aforementioned advantages, low specific surface area and limited electrical conductivity are major problems that must be overcome [82]. The criteria for selecting a suitable metal oxide to decorate carbon-based materials for an electrochemical system include the following [83]:

1. excellent chemical stability in acidic or alkaline electrolyte
2. high conductivity to facilitate electron transfer
3. good durability to withstand corrosion and degradation during operation
4. high specific surface area to facilitate access to and from the substrate and generate high current
5. good adhesion to substrate
6. porous structure to boost mass transfer between electrolyte and electrode surface and obtain high specific surface area
7. low cost

The fabrication of metal oxide electrocatalysts can be achieved through a variety of modification methods. Table 3.1 summarizes the most common methods used to form metal oxide electrocatalysts on carbon-based electrodes.

Table 3.1: List of the synthesis methods for metal oxide electrocatalysts

Synthesis method	**Method description**	**Advantages**	**Drawbacks**	**Ref.**
Hydrothermal	Aqueous solution used to form inorganic nanomaterials. Precursor concentration, temperature, pH and pressure are manipulated varibales. Water is used as solvent.	Cost-effective, eco-friendly, versatile, and simple 1-step preparation. Safe and does not require H_2. Morphology, composition, and crystallinity of nanomaterials can be controlled.	High energy consumption.	[84, 9]

Table 3.1 continued from previous page

Synthesis method	Method description	Advantages	Drawbacks	Ref.
Solvothermal	Ethanol and ethylene glycol used as solvents and reductant instead of water. Solvent and surfactant type, pH, precursor concentration, operating conditions (T and P) and occupied volume of autoclave, are the controlling factors.	In addition to the advantages of hydrothermal methods, solvothermal method requires lower temperatures and shorter periods of heat treatment. Ethanol solvent contributes to lower operating temperature by providing multifunctional property to modify morphology.	Environmental issues.	[84]

Table 3.1 continued from previous page

Synthesis method	Method description	Advantages	Drawbacks	Ref.
Electrospinning	Viscoelastic, polymeric mixture containing metal oxide salts used to form solid polymer fiber under application of electric field. This followed by calcination to remove polymeric compounds and purify metal oxides.	Adaptable and versatile method for a variety of metal oxides.	Polymer fibre thickness depends on metal oxide precursors and conductivity of mixture.	[9]
Electrodeposition	Metal oxide is deposited on unmodified electrode from electrolyte containing the desired metal ions	Current, electrolyte structure and deposition time control electrocatalyst thickness and grain size. Facile 1-step method.	Morphology of some nanomaterials cannot be controlled using this method.	[9]

Table 3.1 continued from previous page

Synthesis method	Method description	Advantages	Drawbacks	Ref.
Impregnation	Unmodified electrode is immersed in solution containing metal-bearing ions. Ion exchange or adsorption of metal oxide ions take place on the electrode surface. Calcination process is carried out as final step to enhance metal oxide production on electrode surface.	Simple and widely used technique.	Limitations associated with loading and adhesion of metal oxides on electrode surface.	[9]

The scope of this work will be limited to the use of the hydrothermal and solvothermal methods to incorporate metal oxides into GF electrodes. Solvothermal methods have some advantages over hydrothermal methods. They produce higher yields and can be operated at lower temperatures [81]. They involve the use of a teflon-lined stainless steel autoclave in which the metal oxide precursors react with the solvent. Solvothermal treatment is then followed by calcination. As noted by Xiang *et al.*, calcination at higher temperature (>400 C for 2 hr) enhances the wettability of GF electrodes [85]. Furthermore, it helps produce purer metal oxides and improve their adhesion on the electrode surface [9]. Table 3.2 provides a list of different metal oxides (MOs) used to modify GF for various RFB systems. Among the MOs listed in Table 3.2, this work is limited to the deposition of two MOs on the GF surface: namely tungsten trioxide (WO_3), and tin dioxide (SnO_2), on the surface of GF electrode.

Table 3.2: Metal oxides used to optimize GF using hydrothermal and solvothermal methods

Materials	**Method**	**Modification condition**	**RFB System**	**Ref.**
WO_3	Hydrothermal	$Na_2WO_4 \cdot 2H_2O$ precursor is added to aqueous solution containing HCl and $H_2C_2O_4$ and heated at 180 °C for 4 h.	all-vanadium	[56]
$W_{18}O_{49}$	Solvothermal	WCl_6 precursor dissolved in ethanol and heated at 180 °C for 12 h.	all-vanadium	[86]
$Ce_xZr_{1-x}O_2$	Hydrothermal	$Ce(NO_3)_3 \cdot 6H_2O$ and $ZrOCl_2 \cdot 8H_2O$ precursors mixed together with DI water and heated at 200 °C for 8 h.	all-vanadium	[87]
Nb_2O_5	Hydrothermal	Ammonium niobium oxalate dissolved in DI water and maintained at 170 °C for 48 h.	all-vanadium	[88]
MoS_2	Hydrothermal	Sodium molybdate dihydrate and thiourea (CH_4N_2S) mixed with DI water and reacted at 200 °C for 36 h.	all-vanadium	[89]

Table 3.2 continued from previous page

Materials	Method	Modification condition	RFB System	Ref.
Ta_2O_5	Hydrothermal	Ta_2O_5 powder dissolved in 0.1 M HCl at pH 9 using 1 M NH_3 solution. As-prepared solution is then dissolved in mixed solution of 1 M ammonia and 1 M hydrogen peroxide to produce required precursor. Pre-treatment of resulting solution performed in oil bath at 70 °C for 1 h before heating at 240 °C for 12 h in Teflon-lined autoclave.	all-vanadium	[90]
Binary-$NiCoO_2$	Solvothermal	Co(II) nitrate hexahydrate, Ni(II) chloride dissolved in diluted ethanol and heated at 80 °C for 14 h.	all-vanadium	[85]
Niobium-doped hexagonal tungsten trioxide nanowires	Hydrothermal	$Na_2WO_4{\cdot}2H_2O$ dissolved in deionized water and mixed with solution containing $NbCl_5$ solids in ethanol. Then, HCl and ammonium sulfate ($(NH_4)_2SO_4$) added to the resultant solution.	all-vanadium	[75]

Table 3.2 continued from previous page

Materials	Method	Modification condition	RFB System	Ref.
CeO_2	Hydrothermal	$CeCl_3$ and $Na_2PO_4.6H_2O$ dissolved in DI water and heated at 160 °C for 24 h.	all-vanadium	[91]
WO_3	Solvothermal	WCl_6 precursor dissolved in ethanol in presence of F-127 and then heat-treated at 180 °C for 24 h.	cerium-lead	[68]
SnO_2	Solvothermal	Methanol used as solvent to dissolve $SnCl_4.5H_2O$ and then heat-treated at 180 °C for 4 h.		[67]

Chapter 4

EQUIPMENT AND EXPERIMENTAL METHODS

4.1 Materials

All chemicals were used as received without further purification unless stated otherwise. Furthermore, all solutions were prepared with ultra-pure water (resistivity of $\sim 18 M\Omega$ cm). Cerium (III)- methanesulfonate electrolyte was synthesized using appropriate amounts of 99% pure cerium(III) carbonate (Treibacher Industrie AG) and 70% methanesulfonic acid (Sigma Aldrich). 68-70% Nitric acid (BDH) and 95-98% sulfuric acid (Sigma Aldrich) were used as received. 85% nitrogen gas was obtained from Praxair.

In the case of metal oxides preparation, tungsten trioxide (WO_3) was prepared by dissolving both 99.9% tungsten hexachloride (Sigma Aldrich) and 950-1000 ppm Pluronic® F-127 powder (Sigma Aldrich) in a specific volume of absolute ethanol (UW Chem-Store).

98% tin(IV) chloride pentahydrate (Sigma Aldrich) served as the tin oxide precursor along with Pluronic® F-127 (Sigma Aldrich) and dissolved in absolute ethanol (UW Chemistry Store) along with 950-1000 ppm Pluronic© F-127 powder (Sigma Aldrich).

4.2 Electrode Preparation

1. **Purification step**

   Pristine graphite felt (GF, FuelCell Store, AvCarb G475A) with dimensions 2 cm × 3 cm × 4.7 mm (Figure 4.1) was cleaned in an ultrasonic bath with absolute ethanol for 15 minutes and then rinsed with ultra-pure water several times to remove impurities. Subsequently, the graphite felt was dried in a vacuum muffle oven at 200 °C for 30 minutes and denoted as as-received/GF. Without this purification step, Ce(III) oxidation during the anodic scan is severely inhibited, as shown in Figure 4.2. Only once the GF is cleaned with ethanol and ultra-pure water, does the current rise beginning at ∼ 1.2 V vs. Ag|AgCl characteristic of Ce(III) oxidation appear during the anodic scan.

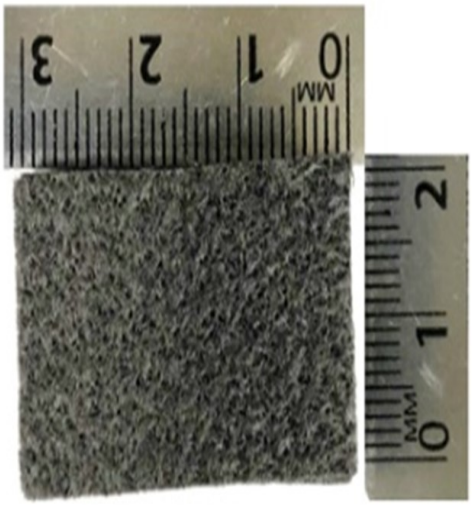

Figure 4.1: Pristine graphite felts (2 cm × 3 cm × 4.7 mm)

2. **Acid activation step**

   In this step, the GF was treated with acid to introduce oxygen-containing functional groups, e.g., phenolic (C-O) and carboxylic (C=O), and nitrogen-containing groups (-NH_2) on its GF surface. This step was conducted to improve GF hydrophilicity, leading to better contact of electrolyte to the electrode surface and a lower energy barrier for the redox reaction at the electrolyte-electrode interface. The acid treatment was carried out by contacting the as-received/GF with 50 ml mixed solution of HNO_3:H_2SO_4 (3:1 v/v). The mixed solution was then transferred into a 100 ml glass Erlenmeyer flask. Next, as-received GF was immersed in the mixed solution and maintained at 80 °C for 4 h using a water bath (Fisher Scientific) without stirring. Then, the treated GF was subjected to repeated water-washing and drying at 100 °C for 1 h using muffle furnace. This acid-treated graphite felt is denoted as AGF.

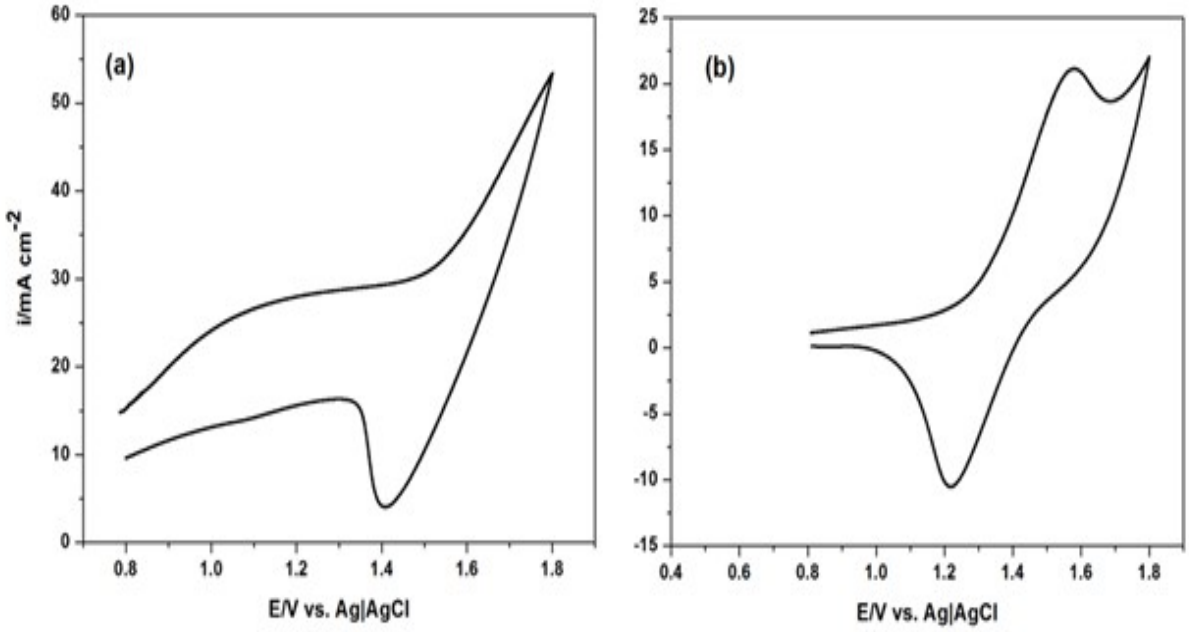

Figure 4.2: Cyclic voltammograms of as-received GF electrode in 0.05 M Ce(III) methanesulfonate + 1.0 M MSA at scan rate of 3 mV s^{-1}, (a) without purification; (b) after purification.

3. **Solvothermal step**

   Figure 4.3 summarizes the major steps for the decoration of the metal oxide nanoparticles on GF surfaces using the solvothermal method.

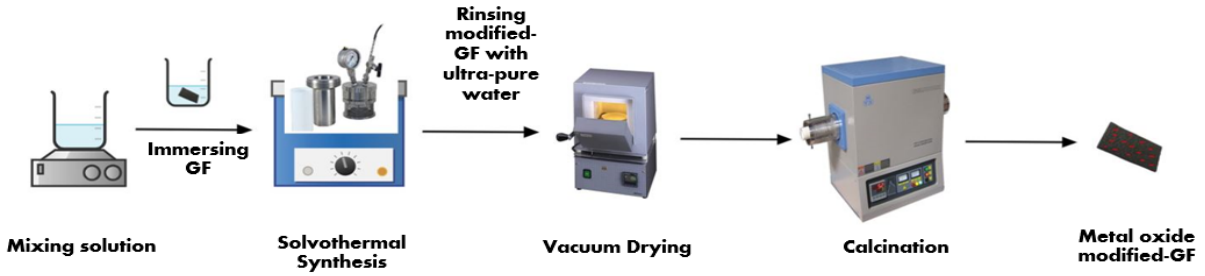

Figure 4.3: Schematic representation for the synthesis of metal oxide nanocomposites onto GF surface using solvothermal route.

A solvothermal step was then carried out to incorporate nanocomposite particles of the various metal oxides (WO_3 and SnO_2) on the AGF surface. In particular, the appropriate amounts of metal oxide precursors (see Chapter 5) were dissolved in the 50 ml ethanol solvent and subjected to constant stirring via a magnetic stirrer for 1 h at room temperature. Then, this solution was transferred to the PTFE insert contained within a 100 ml steel mini-autoclave (Buchiglas USA Corp). Following this step, the AGF was immersed in the solution for the solvothermal treatment at 180 °C for 24 h using an oil bath (KISS 208B, Buchiglas USA Corp). After the contents of the autoclave were allowed to cool down to room temperature, the treated graphite felt was removed and rinsed with ultra-pure water several times and vacuum-dried in a muffle furnace at 100 °C for 1 h. This sample is denoted as W/GF or Sn/GF, depending on the deposited metal oxide. In this step, the amount of metal oxide precursors added to AGF was varied and the electrochemical performance of the resulting electrodes for the Ce(III)/Ce(IV) reaction was evaluated to determine the optimum formulation.

4. **Calcination step**

   The calcination step is usually referred as the activation step and yields the desired metal oxide product on the GF surface. This step involved the calcination of the GF sample obtained from the previous step at 500 °C for 2 h at a rate of 2 °C min^{-1} under nitrogen flow in a tubular furnace. After removal from this furnace, the treated GF was thoroughly rinsed with ultra-pure water and vacuum-dried at 200 °C for 30 minutes in a muffle oven. Finally, the treated GF samples were stored in plastic bags prior to physicochemical characterization and electrochemical measurements.

4.3 Physicochemical Characterization

The surface morphology of the fibers in graphite felts was analyzed by scanning electron microscopy (SEM, Quanta 250 FEG, FEI) and its elemental content evaluated by energy dispersive X-ray spectroscopy (EDX, INCA X-ACT, Oxford Instruments). X-ray photoelectron spectroscopy (XPS) was also used to characterize the chemical nature (i.e., oxidation state) and composition of the metal oxide components on the modified fiber surfaces from spectra scans of the intensity of the emitted photoelectrons as a function of their binding energy. These XPS spectra were obtained with a Thermo-VG Scientific ESCALab 250 XPS system operating with a monochromatic Al (K-alpha) X-ray source.

4.4 Electrochemical Characterization

Only half-cell electrochemical experiments were conducted to characterize the Ce(III)/Ce(IV) reaction on the GF-modified electrodes in this study. These experiments were carried out using a 3-electrode setup controlled with an EPP-400 Potentiostat (Princeton Applied Research). For the half-cell experiments, cyclic voltammetry (CV) was conducted at room temperature (23 °C) in a 0.05 M Ce(III) MSA + 1.0 M MSA electrolyte using a custom-made three-electrode cell (see Figure 4.4).

Figure 4.4: Custom-made three-electrode cell

The electrolyte composition was chosen based on the results of recently published studies that investigated the use of WO_3 [68] and SnO_2 [67] modified-GFs for cerium-based redox flow batteries. Approximately 25 ml of electrolyte was used during each experiment. In each experiment, a treated graphite felt sample (1 cm × 3 cm) with an active surface area

of 1 cm^2 was used as the working electrode, Ag|AgCl (0.286 V vs. SHE, Pine Research Instrumentation) as the reference electrode and a graphite rod (6.15 mm diameter × 50 mm long) as the counter electrode. In the case of the GF working electrode preparation, green PET tape (Uline) was applied to the electrode to expose an active surface area of 1 cm^2 (see Figure 4.5).

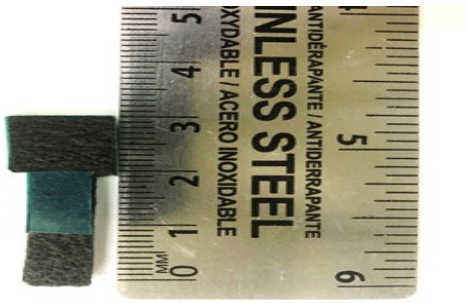

Figure 4.5: Working GF electrode (1 cm^2)

A wire lead housed within a hollow glass rod and connected to the potentiostat was attached to the working electrode using an alligator clip. All electrode potentials reported in this study are reported on the Ag|AgCl scale. The cyclic voltammograms were obtained over the voltage range from 0.56 to 1.8 V vs. Ag|AgCl at a scan rate of 3 mV s^{-1}. Note that the electrolyte does not initially contain any Ce(IV) in these experiments. Ce(IV) is produced only as a result for Ce(III) oxidation during the anodic scan of each CV run. The open-circuit voltage (OCV) of the positive half-cell of Zn-Ce RFB using as-received GF was measured experimentally and found to be 0.56V vs. Ag|AgCl in 0.05 M Ce(III) MSA + 1.0 M MSA electrolyte at room temperature prior to CV and the formation of any Ce(IV). The lower potential for the CV experiments in this study was chosen to be 0.56 V vs. Ag|AgCl, while the upper potential was set to 1.8 V vs. Ag|AgCl to ensure the oxidation of Ce(III) to Ce(IV) which takes place at a standard potential of 1.72 V vs.

Ag|AgCl. The durability of the modified GF electrodes was assessed by subjecting them to multiple CV cycles over the voltage range from 0.56 to 1.8 V vs. Ag|AgCl at a scan rate of 10 mV s^{-1}. In this study, the CV experiments were conducted at low scan rates (3 and 10 mV s^{-1}) to provide enough time for redox ions to penetrate deeply into pores, produce high charge and high specific capacitance [92]. In this study, the ratio of the cathodic peak current density to the anodic peak current density (I_{pc}/I_{pa}), peak potential separation (ΔE_p) and coulombic charge obtained from the CVs were used to evaluate the activity and reversibility of the Ce(III)/Ce(IV) reaction on the various GF electrode samples.

Chapter 5

RESULTS AND DISCUSSION

5.1 Electrochemical Measurements

Cyclic voltammetry (CV) was conducted to characterize the rate of the Ce(III)/Ce(IV) redox reaction occurring on various GF-based electrodes. These CV experiments were conducted at $\sim$ 23 °C in a 0.05M Ce(III) MSA + 1.0 M MSA electrolyte using a custom-made three-electrode cell. The half-cell electrochemical experiments were carried out over the potential range from 0.56 to 1.8 V vs. Ag|AgCl at a scan rate of 3 mV s^{-1}. The stability of the electrodes was assessed by subjecting them to multiple CV cycles over the potential range from 0.56 to 1.8 V vs. Ag|AgCl at a scan rate of 10 mV s^{-1}.

5.1.1 Cyclic Voltammetry Analysis

5.1.1.1 Comparison of Pt and unmodified GF electrodes for Ce(III)-Ce(IV) reaction

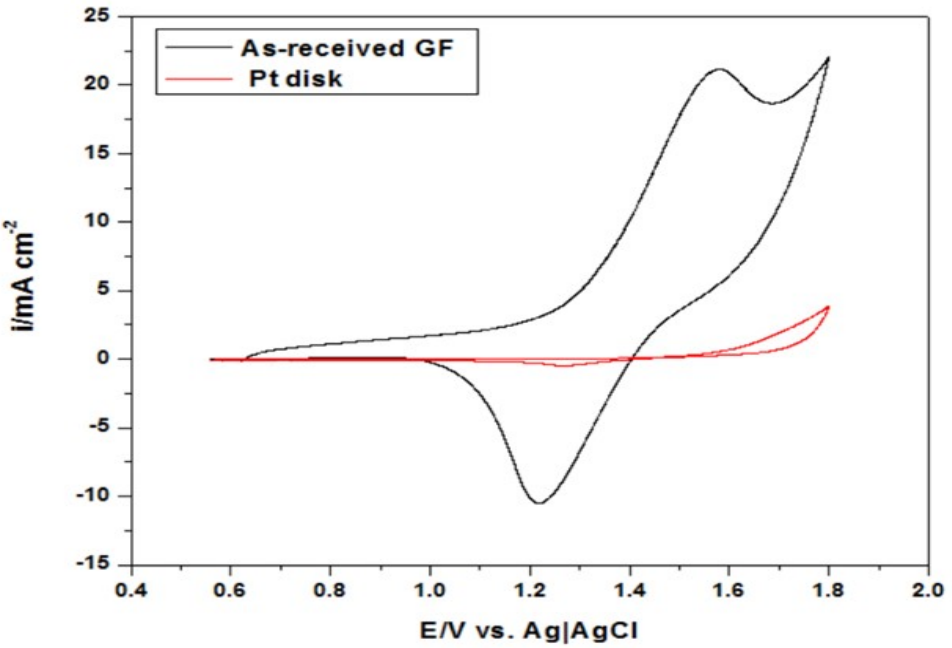

Figure 5.1: Cyclic voltammograms for the Ce(III)/Ce(IV) redox couple in 0.05M Ce(III) MSA + 1.0 M MSA electrolyte at platinum (Pt) and pristine graphite felt (GF) electrodes at room temperature. The electrode potential was swept from 0.56 to +1.8V vs. Ag|AgCl then from +1.8 to 0.56V vs. Ag|AgCl at 3 mV s^{-1}.

Figure 5.1 presents the cyclic voltammograms obtained at a scan rate of 3 mV s^{-1} on platinum (Pt) disk (diameter = 7.5 mm) and as-received graphite felt (GF) electrodes in an electrolyte containing 0.05M Ce(III) MSA + 1.0 M MSA at 23 °C. The superficial areas of

the Pt disk and as-received GF are 0.44 cm^2 and 1.0 cm^2, respectively. As shown in Figure 5.1, the current density on Pt continually rises to a maximum of 2.9 mA cm^{-2} by the end of the anodic scan, whereas the current density rises much more steeply beginning close to 1.2V vs. Ag|AgCl and reaches a well-defined peak I_{pa} at 21.1 mA cm^{-2} on GF. The peak current densities I_{pc} for Ce(IV) reduction on Pt and GF are found to be 0.4 and 10.5 mA cm^{-2}, respectively. Based on these values, the ratio I_{pc}/I_{pa} of the peak current densities on Pt and GF are calculated to be 0.12 and 0.49, respectively. These observations indicate that the kinetics for Ce(III) oxidation are much more facile on GF. Also, the separation between the anodic and cathodic peak potentials observed on GF is 0.42 compared to 0.52 V on Pt. These trends indicate that the unmodified GF exhibits superior performance toward the Ce(III)/Ce(IV) reaction compared to the Pt disk electrode. These findings are in line with those of previous studies that evaluated kinetics of Ce(III)/Ce(IV) reaction on both Pt and carbon-based electrodes (i.e. glassy carbon, graphite felt etc.) using data obtained from CV curves [26, 31, 45, 32, 37]. In making this comparison, one must be careful since the GF electrode has a porous structure presumably with a larger surface area than the Pt disk which has a planar surface. Thus, it is difficult to conclude how much of the difference in the electrode responses on the two electrodes in Figure 5.1 is due to surface area effects and how much (if any) is due to electrocatalytic activity. In particular, a smaller peak separation and higher peak current density would serve as indicators of improved kinetic activity if all the tested electrodes possess the same surface structure, which does not apply in this case. Thus, peak separation and peak current density obtained from CVs alone should not be used as indicators to assess kinetic activity of an electrode, particularly when comparing porous GF and planar Pt electrodes. Obviously, it would be best to independently measure the surface area of the porous GF electrodes when comparing their performance to that of

planar Pt.

5.1.1.2 WO_3 nanoparticle-modified graphite felts

WO_3 has distinctive optical and electronic features that have opened up a number of applications such as catalysis, gas sensing, energy storage and electrochemistry [9, 75]. In addition, WO_3 is stable in acidic media, non-toxic and readily available [68]. However, WO_3 exhibits poor electrical conductivity, which limits its energy storage capability [93]. Na *et al.* investigated the electrocatalytic effect of WO_3/GF on Ce(III)/Ce(IV) reversibility in a cerium-lead RFB. Although they found that this electrode exhibited promising electrochemical performance and stability, the WO_3/GF structure was found to have a disordered orientation and close packing, leading to a reduced number of active sites and lower specific area [68]. A solvothermal method was used to form WO_3 nanoparticles on a GF surface. WCl_6 precursor which served as a source of WO_3 was dissolved in ethanol in presence of F-127 and then heat-treated at 180 °C for 24 h. It was found that electrochemical activity and stability of GF were enhanced significantly after WO_3 decoration. Additionally, the energy efficiency of the WO_3-modified GF operating at a charge/discharge rate of 30 mA cm^{-2} increased by 41.1% compared to that obtained on unmodified GF [68]. In our study, the incorporation of WO_3 onto the GF surface was conducted using the solvothermal method at 180 °C for 24 h. Different amounts of 99.9% tungsten hexachloride (WCl_6) and 950-1000 ppm Pluronic F-127 powder were dissolved in 50 ml absolute ethanol while continuously agitating with a magnetic stirrer for 1 h at room temperature. F-127 was added as a surfactant to enhance adhesion of the hydrophilic metal oxide layer to the relatively hydrophobic GF surface. Table 5.1 lists the amounts of WCl_6 and F-127 added to produce

Table 5.1: Modified GFs with different contents of WCl_6

Electrode	**WCl_6 (g)**	**F-127 (g)**
0.1 M W/GF	1.98	1.98
0.07M W/GF	1.39	1.39
0.05M W/GF	0.99	0.99

the three modified GF electrodes evaluated in this study. These electrodes are denoted in terms of the WCl_6 molar concentration in the ethanol solution treated in the autoclave.

For this analysis, the ratio of the reduction peak current density to the anodic peak current density (I_{pc}/I_{pa}), peak potential separation (ΔE_p) and the ratio between anodic and cathodic charges (Q_a/Q_c) obtained from the CVs are used to evaluate the activity and reversibility of the Ce(III)/Ce(IV) reaction on the three GF electrodes above. The differences in the surface areas of these electrodes should not be large enough to invalidate the use of these parameters alone (i.e., without measuring the surface area of each electrode) as measures of the electrocatalytic activity and reaction reversibility.

Figure 5.2 presents the CVs obtained on as-received GF and W/GF at a scan rate of 3 mV s^{-1} in 0.05M Ce(III) MSA + 1.0 M MSA electrolyte. Comparison of the electrode responses shows some enhancement in the electrochemical performance of as-received GF after WO_3 decoration. For instance, I_{pa} and I_{pc} on 0.07M W/GF are 24.75 mA/cm^{-2} and 20.44 mA/cm^{-2}, respectively, compared to only 21.14 mA/cm^{-2} and 10.51 mA/cm^{-2}, respectively, in the case of as-received GF (Table 5.2). A comparison of I_{pa} values is complicated by the fact that both Ce(III) oxidation and O_2 evolution can occur during the anodic scan. However, a measure of the extent of Ce(III) oxidation during the anodic scan

can determined from the size of the cathodic peak for Ce(IV) reduction observed during the subsequent cathodic scan since Ce(IV) is present in the system only as a result of Ce(III) oxidation. If I_{pc} is used as a measure of the amount of Ce(IV) reduction, the amount of Ce(III) oxidation during the anodic scan decreases in the following order: 0.07 M W/GF > 0.1 M W/GF > 0.05 M W/GF > GF. Based on these trends, an intermediate level of WCl_6 in the precursor solution yields the best electrocatalytic activity in the resulting modified GF electrode.

Measures of the reversibility of the Ce(III)/Ce(IV) reaction can be obtained from the I_{pc}/I_{pa} ratio and separation between the anodic and cathodic peaks. The I_{pc}/I_{pa} ratio obtained on 0.07 M W/GF, 0.1 M W/GF and 0.05 M W/GF are estimated to be 0.83, 0.77 and 0.72, respectively, which are closer to 1 than the value of 0.49 measured on as-received GF. However, the peak separations do not follow this trend which decrease in the order: 0.05M W/GF (0.72 V) > 0.07M W/GF (0.53 V) > 0.1M W/GF (0.46 V) > GF (0.42 V).

Another measure of the extent of the various reactions is the coulombic charge associated with the anodic and cathodic processes on each electrode. Accordingly, we have measured the area under each of the CVs. Table 5.3 shows the charge Q_a obtained during the anodic scan and the charge Q_c during the reverse scan on the various GFs. The anodic charge over the potential range from $\sim$ 1.1V to 1.8V was determined, while the cathodic charge was obtained over the potential range from $\sim$ 0.56V to 1.4V. As evident from Table 5.3, Q_a increases from 3.71 C to 4.16 C when as-received GF is modified with 0.07M W. This provides a possible indication that the kinetics of Ce(III) oxidation is facilitated by WO_3 modification. Most importantly, Q_c obtained on 0.07M W/GF is the highest among

all GF samples. This suggests that the amount of Ce(IV) formed during the anodic scan on 0.07M W/GF (1.58 C) electrode is enhanced significantly compared to that on as-received GF (0.66 C). The Q_c/Q_a ratios for all GFs are also shown in Table 5.3. As can be seen from the table (below), 0.05M W/GF (48.3 %) exhibits the highest Q_c/Q_a ratio among all modified GFs, indicating that reversibility of Ce(III)/Ce(IV) was improved significantly on this electrode compared to as-received GF (17.8 %). Although the findings obtained on the basis of the Q_c/Q_a ratios regarding the reversibility of Ce(III)/Ce(IV) do not support those obtained from the peak separation, the Q_c/Q_a ratio may serve as the best measure of redox species reversibility, especially for porous electrodes [9]. Overall, the improvement of the electrochemical activity of the modified GFs toward the Ce(III)/Ce(IV) reaction can be attributed to the WO_3 coating which introduces oxygen-containing groups on the GF surface. This should enhance electrolyte access and improve the hydrophilicity of GF after WO_3 modification.

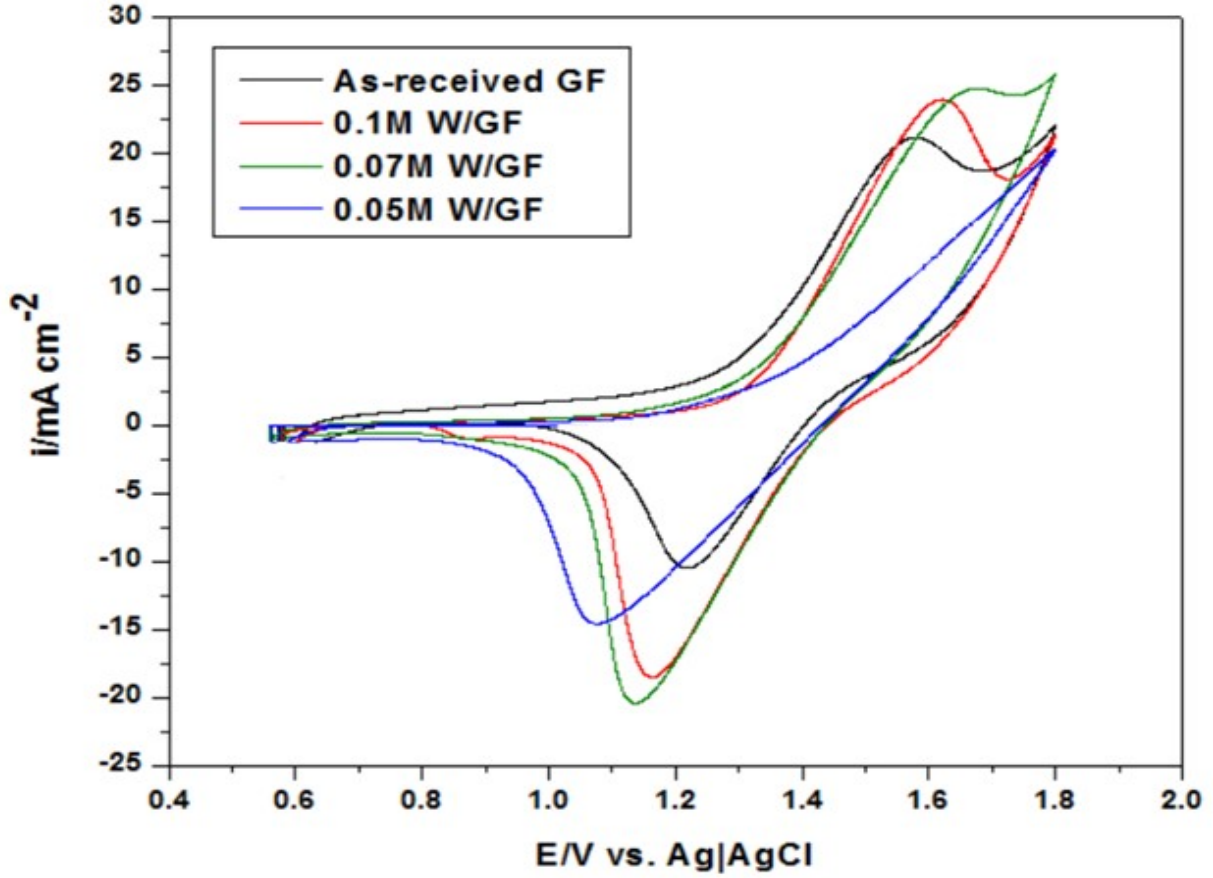

Figure 5.2: Cyclic voltammograms for the Ce(III)/Ce(IV) redox couple in 0.05M Ce(III) MSA + 1.0 M MSA electrolyte at pristine graphite felt (GF) and WO_3 modified-GFs electrodes at room temperature. The electrode potential was swept from 0.56 to +1.8V vs. Ag|AgCl then from +1.8 to 0.56V vs. Ag|AgCl at 3 mV s^{-1}.

Table 5.2: Electrochemical parameters obtained from the CV curves in Figure 5.2 for the Ce(III)/Ce(IV) redox reaction on various modified GFs with WO_3 at scan rate of 3 mV s^{-1}

Electrode	**Peak current density (mA cm^{-2})**		**Peak potential (V)**		**I_{pc}/I_{pa}**	**ΔE_p (V)**
	I_{pa}	**I_{pc}**	**E_{pa}**	**E_{pc}**		
As-received GF	21.1	10.5	1.6	1.2	0.5	0.4
0.1M W/GF	24.0	18.5	1.6	1.2	0.8	0.5
0.07M W/GF	24.8	20.4	1.7	1.1	0.8	0.5
0.05M W/GF	20.3	14.6	1.8	1.1	0.7	0.7

Table 5.3: Anodic and cathodic charges obtained in the potential ranges of 1.1V - 1.8V and 0.56V - 1.4V, respectively from integrating the area under CV curves in Figure 5.2 for the Ce(III)/Ce(IV) redox reaction on various modified GFs with WO_3 at scan rate of 3 mVs^{-1}

Electrode	**Charge (C)**		**Q_c/Q_a x 100%**
	Q_a	Q_c	
As-received GF	3.7	0.7	17.8
0.1M W/GF	3.6	1.3	36.7
0.07M W/GF	4.2	1.6	38.0
0.05M W/GF	2.9	1.4	48.3

5.1.1.3 SnO_2 nanoparticle-modified graphite felt

Tin dioxide (SnO_2) has been extensively utilized as a catalytic support in several energy storage applications because of its outstanding resistance to corrosion at severe acidic media. It also has demonstrated good electrocatalytic activity at highly positive potentials and is relatively inexpensive [9, 67]. SnO_2 was decorated on GF using a solvothermal method at 180 °C for 24 h. The $SnCl_4.5H_2O$ precursor was dissolved in 50 ml ethanol with F-127 in various amounts and then stirred for 1 hour at room temperature. The different formulations of the electrode composition were obtained by varying the amount of $SnCl_4.5H_2O$ used, as shown in Table 5.4. The electrodes are designated in terms of the $SnCl_4.5H_2O$ concentration in the ethanol solution treated in the autoclave.

Table 5.4: GFs modified with different amounts of $SnCl_4.5H_2O$

Electrode	**$SnCl_4.5H_2O$ (g)**	**F-127 (g)**
0.1 M Sn/GF	1.76	1.76
0.07M Sn/GF	1.23	1.23
0.05M Sn/GF	0.88	0.88

As shown in Figure 5.3, CVs obtained on as-received GF and the Sn/GF electrodes were obtained at a scan rate of 3 mV s^{-1} in 0.05M Ce(III) MSA + 1.0 M MSA electrolyte at room temperature. Analysis of these responses yields the data shown in Tables 5.5 and 5.6. Based on the various measures, 0.05M Sn/GF clearly exhibits the best electrochemical activity toward Ce(III)/Ce(IV) redox reaction among the three modified Sn/GFs and a significant improvement over that obtained using unmodified GF. Interestingly, the use of more $SnCl_4.5H_2O$ in the precursor than 0.05M Sn does not lead to better results

and, in fact, leads to poorer behaviour than unmodified GF. The ratio of the redox peak current density (I_{pc}/I_{pa}) is found to be 0.10 and 0.31 for 0.1 M Sn/GF and 0.07M Sn/GF, respectively, compared with 0.49 for GF. As in the case with tungsten oxide modification, these trends suggest that an intermediate amount of tin oxide yields the highest activity toward the Ce(III)/Ce(IV) reaction. Modification with tin oxide also leads to a larger peak separation, also similar to what is observed with tungsten oxide modification. The peak separation obtained on the different GFs decreases in the order: 0.05M Sn/GF (0.68 V) > 0.1M Sn/GF (0.61 V) > 0.07M Sn/GF (0.58 V) > GF (0.42 V).

Table 5.6 compares Q_a and Q_c for SnO_2-modified GFs to that of as-received GF in the potential ranges from 1.1V to 1.8V and from 0.56V to 1.4V, respectively. If Q_c is used as a measure of the amount of Ce(IV) produced during the anodic scan, the data indicate that the 0.05M Sn/GF electrode exhibits significantly better activity for Ce(III) oxidation (1.70 C) than the other modified electrodes and unmodified GF. This observation is consistent with the previous conclusion reached on the basis of comparing I_{pa} values (Table 5.5). Thus, it appears that modification with 0.05M Sn leads to improved activity for the Ce(III)/Ce(IV) reaction.

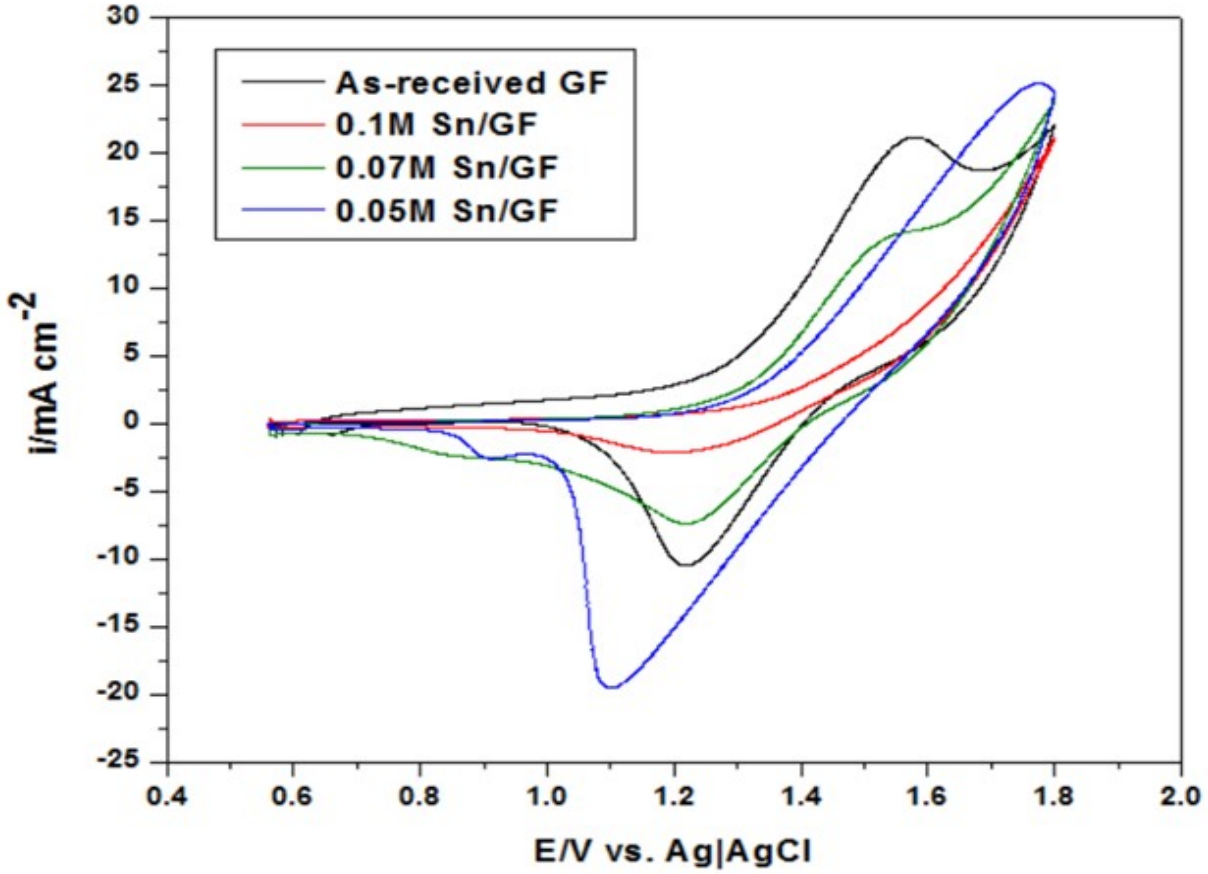

Figure 5.3: Cyclic voltammograms for the Ce(III)/Ce(IV) redox couple in 0.05M Ce(III) MSA + 1.0 M MSA electrolyte at pristine graphite felt (GF) and SnO_2 modified-GFs electrodes at room temperature. The electrode potential was swept from 0.56 to +1.8V vs. Ag|AgCl then from +1.8 to 0.56V vs. Ag|AgCl at 3 mV s^{-1}.

Table 5.5: Electrochemical parameters obtained from the CV curves in Figure 5.3 for the Ce(III)/Ce(IV) redox reaction on various modified GFs with SnO_2 at scan rate of 3 mV s^{-1}

Electrode	**Peak current density (mA cm^{-2})**		**Peak potential (V)**		**I_{pc}/I_{pa}**	**ΔE_p (V)**
	I_{pa}	**I_{pc}**	**E_{pa}**	**E_{pc}**		
As-received GF	21.1	10.5	1.6	1.2	0.5	0.4
0.1M Sn/GF	21.1	2.2	1.8	1.2	0.1	0.6
0.07M Sn/GF	23.9	7.4	1.8	1.2	0.3	0.6
0.05M Sn/GF	25.1	19.6	1.8	1.1	0.8	0.7

Table 5.6: Anodic and cathodic charges obtained in the potential ranges of 1.1V - 1.8V and 0.56V - 1.4V, respectively from integrating the area under CV curves in Figure 5.3 for the Ce(III)/Ce(IV) redox reaction on various modified GFs with SnO_2 at scan rate of 3 mVs^{-1}

Electrode	**Charge (C)**		**Q_c/Q_a x 100%**
	Q_a	**Q_c**	
As-received GF	3.7	0.7	17.8
0.1M Sn/GF	2.5	0.2	7.6
0.07M Sn/GF	3.3	0.7	22.4
0.05M Sn/GF	3.5	1.7	48.0

5.1.1.4 Binary WO_3/SnO_2 nanoparticle-modified graphite felt

A binary mixture of WO_3 and SnO_2 was then used as a novel candidate to improve the electrochemical activity of pristine graphite felts (GFs) for the Ce(III)/Ce(IV) reaction. To the best of our knowledge, no prior studies have reported the use of such a WO_3-SnO_2 binary metal oxide nanocomposite as a potential catalyst for the Ce(III)/Ce(IV) reaction in RFB systems. Previous studies have proposed the use of binary mixture of WO_3 and SnO_2 for gas sensing technology [94], lithium-ion batteries [95] and supercapacitors [96]. In this study, we prepared the mixed WO_3-SnO_2 electrocatalyst using a single-step solvothermal method followed by calcination.

WO_3 and SnO_2 were introduced onto the GF surface using a 1-step solvothermal approach at 180 °C for 24 h. WCl_6 and $SnCl_4.5H_2O$ were used as the precursors for WO_3 and SnO_2, respectively. Each precursor was added in the appropriate amount to separate beakers containing 25 ml ethanol and dissolved by stirring continually for 1 h at room temperature. Next, the two solutions were mixed together in a one beaker before adding F-127 to the mixture. After that, the resulting solution was stirred for 30 min at room temperature. Finally, the precursor mixed solution was added to the autoclave along with GF. Table 5.7 lists the different electrode compositions that were evaluated.

The CVs for the Ce (III)/Ce(IV) reaction obtained on the binary WO_3/SnO_2 modified GFs at a scan rate of 3 mV s^{-1} are shown in Figure 5.4. All modified-GF electrodes were immersed in a 0.05M Ce(III) MSA + 1.0 M MSA electrolyte and their responses were compared to that of as-received GF. The electrochemical data extracted from these CVs in Figure 5.4 are presented in Table 5.8. As Tables 5.8 and 5.9 show, all of the WO_3-SnO_2-modified GFs exhibit higher I_{pa}, I_{pc} and Q_c values than the as-received GF

Table 5.7: GF modified with different amounts of WCl_6 and $SnCl_4.5H_2O$ in this study

Electrode	**WCl_6 (g)**	**$SnCl_4.5H_2O$ (g)**	**F-127 (g)**
0.05M W-0.05M Sn/GF	0.50	0.44	0.47
0.05M W-0.025M Sn/GF	0.50	0.22	0.36
0.025M W-0.05M Sn/GF	0.25	0.44	0.34
0.025M W-0.07M Sn/GF	0.25	0.61	0.43
0.05M W-0.07M Sn/GF	0.50	0.61	0.56

electrode, indicating higher activity for the Ce(III)/Ce(IV) reaction. For instance, I_{pa} and I_{pc} are enhanced from 21.1 mA cm^{-2} and 10.5 mA cm^{-2} for pristine GF to 30.8 mA cm^{-2} and 22.6 mA cm^{-2} for 0.025 M W-0.05M Sn/GF, respectively. Similarly, the I_{pc}/I_{pa} ratio is found to be 0.74 for 0.025 M W-0.05M Sn/GF compared to a value of 0.49 for GF. The peak separation of 0.32 V in the case of 0.025 M W-0.05M Sn/GF is also smaller than 0.42 V for GF. The peak separation among the different electrodes decrease in the following order: 0.05 M W-0.05 M Sn/GF (0.67 V) > 0.025 M W-0.07 M Sn/GF (0.62 V) > 0.05 M W- 0.025M Sn/GF (0.60 V) > 0.05 M W- 0.07 M Sn/GF (0.58 V) > GF (0.42 V) > 0.025 M W-0.05M Sn/GF (0.32 V). These results show that 0.025M W-0.05M Sn/GF yields the highest Ce(III)/Ce(IV) reversibility among these WO_3-SnO_2 modified GFs. Table 5.9 lists Q_a and Q_c for all GFs shown in Figure 5.4 integrated over the potential ranges from 0.56V to 1.8V and 1.1V to 1.4V, respectively. Consistent with the other measures, 0.025M W-0.05M Sn/GF exhibits the highest Q_a (5.4 C) among all the GFs tested. Also, it can be seen from the data in Table 5.9 that binary modified GFs exhibit higher Q_c/Q_a compared

to as-received GF, suggesting that Ce(III)/Ce(IV) reversibility is enhanced after binary WO_3-SnO_2 modification.

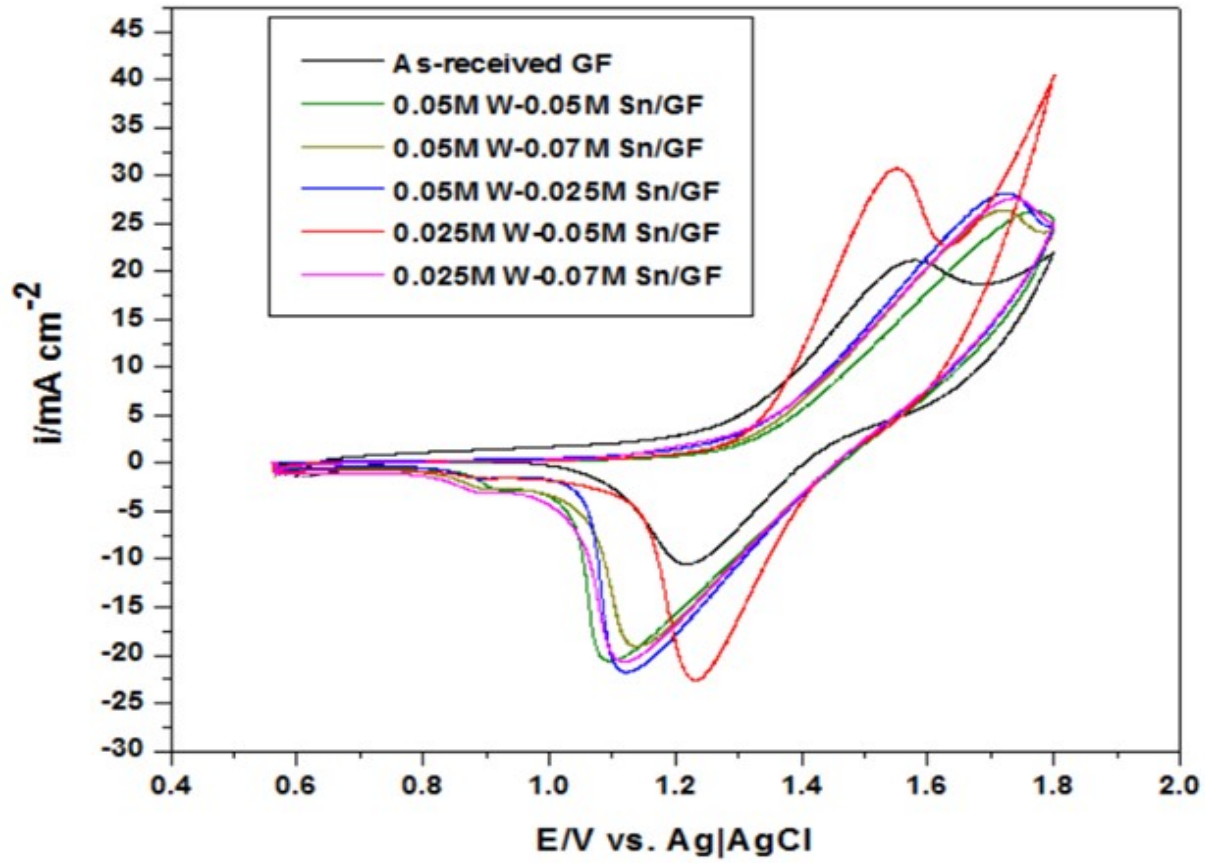

Figure 5.4: Cyclic voltammograms for the Ce(III)/Ce(IV) redox couple in 0.05M Ce(III) MSA + 1.0 M MSA electrolyte at pristine graphite felt (GF) and WO_3/SnO_2 modified-GFs electrodes at room temperature. The electrode potential was swept from 0.56 to +1.8V vs. Ag|AgCl then from +1.8 to 0.56V vs. Ag|AgCl at 3 mV s^{-1}.

Table 5.8: Electrochemical parameters obtained from the CV curves in Figure 5.4 for the Ce(III)/Ce(IV) redox reaction on various modified GFs with binary WO_3-SnO_2 at scan rate of 3 mV s^{-1}

Electrode	**Peak current density (mA cm^{-2})**		**Peak potential (V)**		$\mathbf{I_{pc}/I_{pa}}$	$\mathbf{\Delta E_p}$ **(V)**
	$\mathbf{I_{pa}}$	$\mathbf{I_{pc}}$	$\mathbf{E_{pa}}$	$\mathbf{E_{pc}}$		
As-received GF	21.1	10.5	1.6	1.2	0.5	0.4
0.05M W-0.05M Sn/GF	26.3	20.6	1.8	1.1	0.8	0.7
0.05M W-0.025M Sn/GF	28.2	21.8	1.7	1.1	0.8	0.6
0.025M W-0.05M Sn/GF	30.8	22.6	1.6	1.2	0.7	0.3
0.025M W-0.07M Sn/GF	27.6	20.7	1.7	1.1	0.8	0.6
0.05M W-0.07M Sn/GF	26.4	19.1	1.7	1.1	0.7	0.6

Figure 5.5 presents a comparison of the CVs for single metal-modified GFs (0.07 M W/GF and 0.05 M Sn/GF) and binary metal-modified GF (0.025M W-0.05M Sn/GF) at a scan rate of 3 mV s^{-1}. These particular electrodes have been selected for comparison since they exhibit the highest activity for Ce(III) oxidation among their groups. As clearly evident, the binary 0.025M W-0.05M Sn/GF exhibits superior electrochemical activity compared to the single 0.07M W/GF and 0.05M Sn/GF. The faster kinetics of the Ce(III)/Ce(IV) reaction on the binary 0.025M W-0.05M Sn/GF is demonstrated by the significantly steeper rise in current for the oxidation and reduction processes during both scans than those obtained for 0.07M W/GF and 0.05M Sn/GF. Presumably, this can be attributed to the involvement of both metal oxides (WO_3 and SnO_2) in enhancing the electrochemical kinetics and the reversibility of Ce(III)/Ce(IV).

Table 5.9: Anodic and cathodic charges obtained Figure 5.4 in the potential ranges from 0.56V to 1.8V and 1.1V to 1.4V, respectively, for the Ce(III)/Ce(IV) redox reaction on various modified GFs with binary WO_3-SnO_2 at scan rate of 3 mV s^{-1}

Electrode	**Charge (C)**		**Q_c/Q_a x 100%**
	Q_a	**Q_c**	
As-received GF	3.7	0.7	17.8
0.05M W- 0.05M Sn/GF	3.6	1.8	50.1
0.05M W- 0.025M Sn/GF	4.1	1.7	42.1
0.025M W- 0.05M Sn/GF	5.4	1.5	28.4
0.025M W- 0.07M Sn/GF	4.0	1.9	46.3
0.05M W- 0.07M Sn/GF	3.9	1.7	42.5

Table 5.10 provides a summary of the electrochemical data based on the best anodic charge, cathodic charge and Q_c/Q_a obtained for the as-received GF, WO_3, SnO_2 and binary WO_3-SnO_2 modified GFs. Among all GF samples, the binary WO_3-SnO_2 modified GF exhibits the highest values of Q_a, Q_c and Q_c/Q_a. For example, Q_c/Q_a of as-received GF is found to improve from 17.8% to 50.1% when modified with 0.05M W and 0.05M Sn. This implies that the modification using WO_3 and SnO_2 together enhances the Ce(III)/Ce(IV) reaction more than when WO_3 or SnO_2 alone are used.

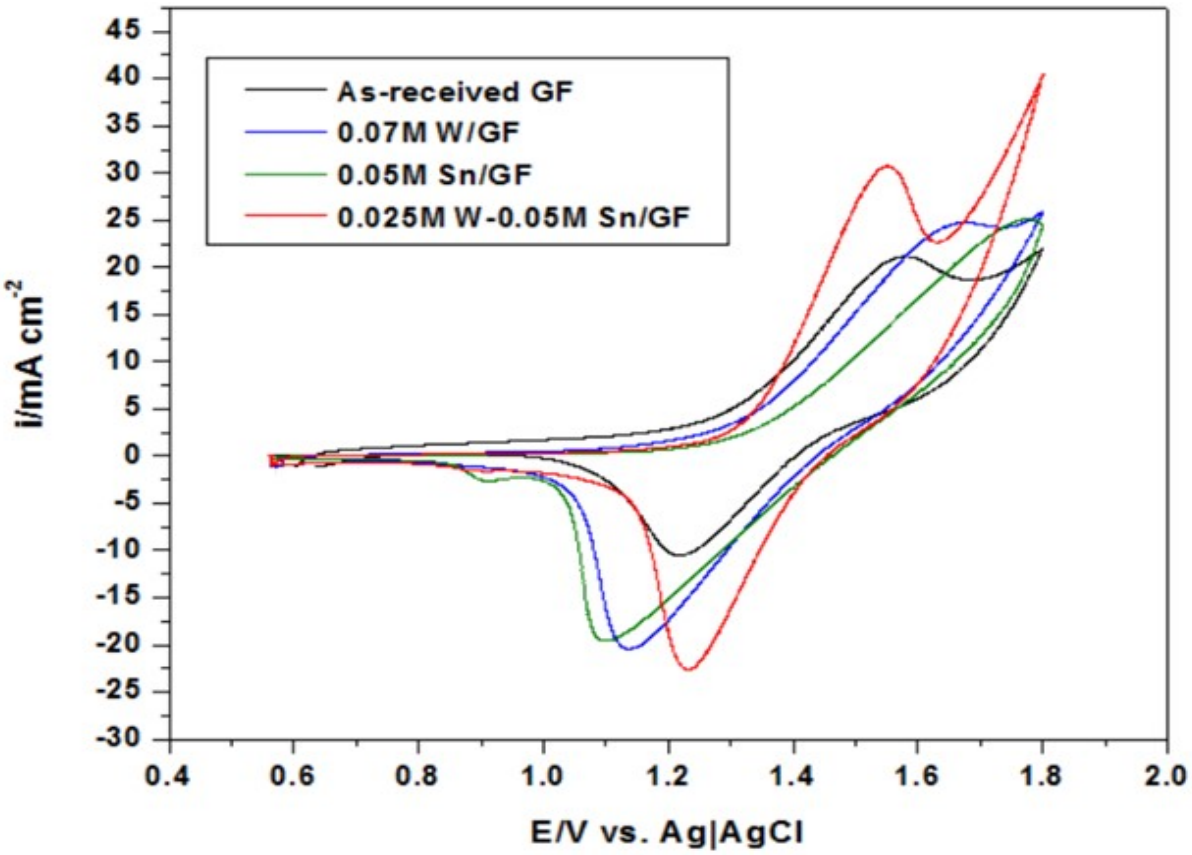

Figure 5.5: A comparison of cyclic voltammograms for the Ce(III)/Ce(IV) redox couple in 0.05M Ce(III) MSA + 1.0 M MSA electrolyte on singular 0.07M W and 0.05M Sn modified GFs, and binary 0.025M W-0.05M Sn modified-GFs electrode at room temperature. The electrode potential was swept from 0.56 to +1.8V vs. Ag|AgCl then from +1.8 to 0.56V vs. Ag|AgCl at 3 mV s^{-1}.

These results indicate that the formation of the binary tungsten oxide-tin oxide composite on GF promotes the Ce(III)/Ce(IV) reaction. Presumably, the introduction of oxygen-containing groups on GF plays an important role in enhancing the electrochemical

Table 5.10: Summary of electrochemical data for the Ce(III)/Ce(IV) redox reaction on various modified GFs at scan rate of 3 mV s^{-1}.

Parameter	**Electrode order (from lowest to highest values)**			
Anodic charge (Q_a)	0.05M Sn/GF	As-received GF	0.07M W/GF	0.025M W-0.05M Sn/GF
[C]	(3.5 C)	(3.7 C)	(4.2 C)	(5.4 C)
Cathodic charge (Q_c)	As-received GF	0.07M W/GF	0.05M Sn/GF	0.025M W-0.07M Sn/GF
[C]	(0.7 C)	(1.6 C)	(1.7 C)	(1.9 C)
Q_c/Q_a x 100	As-received GF	0.05M Sn/GF	0.05M W/GF	0.05M W-0.05M Sn/GF
[%]	(17.8 %)	(48.0 %)	(48.3 %)	(50.1 %)

kinetics and reversibility of Ce(III)/Ce(IV) reactions. These results are consistent with those of other studies where binary oxides were used for other applications (i.e., supercapacitor, all-vanadium redox flow batteries, solid-state gas sensors etc.) [97] [94] [85] [98] [99] and suggest that the use of binary metal oxides promotes some type of synergy between the oxides that further catalyzes redox reactions.

5.1.2 Durability Test

Electrode durability was evaluated using repeated CV cycles over the potential range from 0.56 to 1.8 V vs. Ag|AgCl at a scan rate of 10 mV s^{-1} at room temperature. Figure 5.6 shows the responses obtained by subjecting GF, 0.07M W/GF, 0.05M Sn/GF and 0.025M W-0.05 M Sn/GF to 50 consecutive cycles at a scan rate of 10 mV s^{-1} within the potential window from 0.56 to 1.8 V vs. Ag|AgCl at room temperature for approximately 3 h. As shown in Figure 5.6, the current density changes in different ways depending on the electrode potential over the course of the 50 cycles. In all cases, the cathodic peak current density for Ce(IV) reduction continually shrinks as the CVs continue from the 1^{st} to 50^{th} cycle. The decrease in the amount of Ce(IV) reduction over the 50 cycles occurs for a number of reasons. First, the amount of Ce(III) oxidation during the anodic scans steadily declines. Secondly, some of the Ce(IV) diffuses away from the electrode as it is produced during the anodic scan. Once it diffuses away from the electrode, it can no longer react at the electrode during the cathodic scan. In addition, it is possible that some Ce(IV) oxidizes the carbon on the electrode. In addition to degrading the electrode, this consumes Ce(IV), but does not generate any current during the cathodic scan. Since well-defined peaks are not observed during the anodic scans, it may be more meaningful to determine the anodic charge by integrating under the CVs. Table 5.11 lists the anodic and cathodic charges passed during the 1^{st} and 50^{th} cycles for various GFs obtained by integrating the corresponding CVs. Among all tested electrodes, the binary 0.025M W-0.05 M Sn/GF electrode exhibits the most stable behavior and the lowest anodic and cathodic charge degradation rate of 39.3% and 29.4%, respectively, after 50 cycles (Table 5.11). The electrode responses in Figure 5.6 show that metal oxide modification slows down the

deterioration of the electrochemical performance of GF and extends its lifetime in the oxidizing and acidic electrolyte, but these results also clearly show that their durability remains a problem. In a study investigating the long-term durability of PAN-based graphite felts used as negative electrodes for all-vanadium RFB, Mazur *et al.* performed 2000 charge-discharge cycles [100]. X-ray photoelectron spectroscopy analysis was used to evaluate the changes in surface composition of carbon felts. This study revealed that the performance loss of the negative electrode can be attributed to the decline of sp^2-hybridized carbon and the growth of sp^3-hybridized carbon, leading to a reduction of the conductivity of the GF surface.

Overall, durability of carbon-based materials including graphite felts remains a major problem. Hence, further research is required to further improve the stability of binary metal oxide-modified GF electrodes in the strongly oxidizing environment of the positive electrolyte of Zn-Ce RFBs. Additionally, a deeper understanding of the reaction mechanism and the contribution of various catalysts in enhancing the kinetics of the Ce(III)/Ce(IV) reaction is crucial.

Table 5.11: Degradation of anodic and cathodic charge obtained from Figure 5.6 in the in the potential ranges from 1.1V to 1.8V and 0.56V to 1.4V, respectively, on various GF samples at scan rate of 10 mV s^{-1} and repeated for 50 times.

Electrode	**Anodic charge (C)**			**Cathodic charge (C)**		
	1^{st} cycle	**50^{th} cycle**	**degradation %**	**1^{st} cycle**	**50^{th} cycle**	**degradation %**
GF	3.40	1.71	49.7	0.68	0.01	98.5
0.07M W/GF	3.94	2.17	45.0	1.56	0.97	41.4
0.05M Sn/GF	3.02	1.52	50.0	1.61	0.05	96.9
0.025M W-0.05M Sn/GF	4.89	2.97	39.3	1.87	1.32	29.4

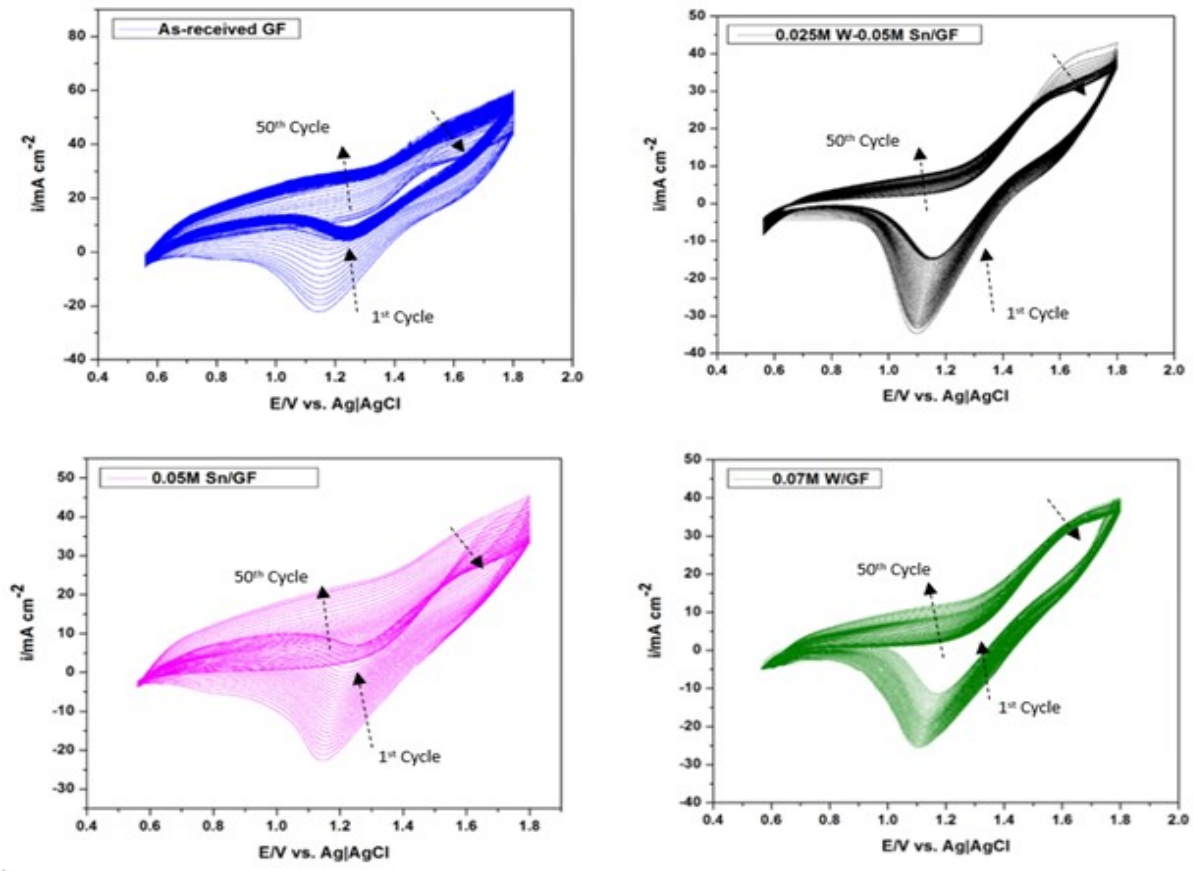

Figure 5.6: Cyclic voltammograms of different GF samples including GF, 0.07M W/GF, 0.05M Sn/GF and 0.025M W-0.05M Sn/GF conducted over the potential window of 0.56 to 1.8 V vs. Ag|AgCl and repeated 50 times for around 3 h at scan rate of 10 mV s^{-1} at room temperature.

5.2 Characterization of Electrode Microstructure and Composition

SEM images of the surface morphology of the various electrodes are shown in Figure 5.7. The presence of the oxides on each of the modified GFs can be clearly seen. Comparison of the images shows that the oxide particles are finer and more uniformly distributed over the GF surface in the case of the binary 0.025M W-0.05M Sn/GF (d and h) than the single metal oxides of 0.07M W/GF (b and f) and 0.05M Sn/GF (c and g). These results suggest that the combination of WO_3 and SnO_2 promotes a more homogeneous dispersion over the GF surface and prevents clustering of the oxide particles that is more evident in the case of the single metal catalysts. In this way, more of the GF surface is catalyzed by the oxide. This difference in the distribution of the oxides is consistent with another observation during the experiments. Figure 5.8a shows a photograph of a beaker containing 0.63 mmol WCl_6 added to 25 ml ethanol along with 0.013 mmol F-127 powder after continual stirring for 1 h at room temperature. Figure 5.8b presents the corresponding photograph of a beaker containing 1.3 mmol $SnCl_4.5H_2O$ and 0.013 mmol F-127 in 25 ml ethanol after continual stirring for 1 h at room temperature.

Figures 5.8c and d show two different views of the remaining precipitate in Figure 5.8a. These images clearly show that a considerable amount of F-127 powder remains undissolved when mixing with WCl_6 solution. However, after mixing the contents of both beakers (Figures 5.8a and b) together, the amount of solids remaining is reduced significantly and a homogeneous solution has been obtained (Figures 5.8e and f). These results confirm that the addition of $SnCl_4.5H_2O$ maintains a high solubility of F-127 powder, suggesting

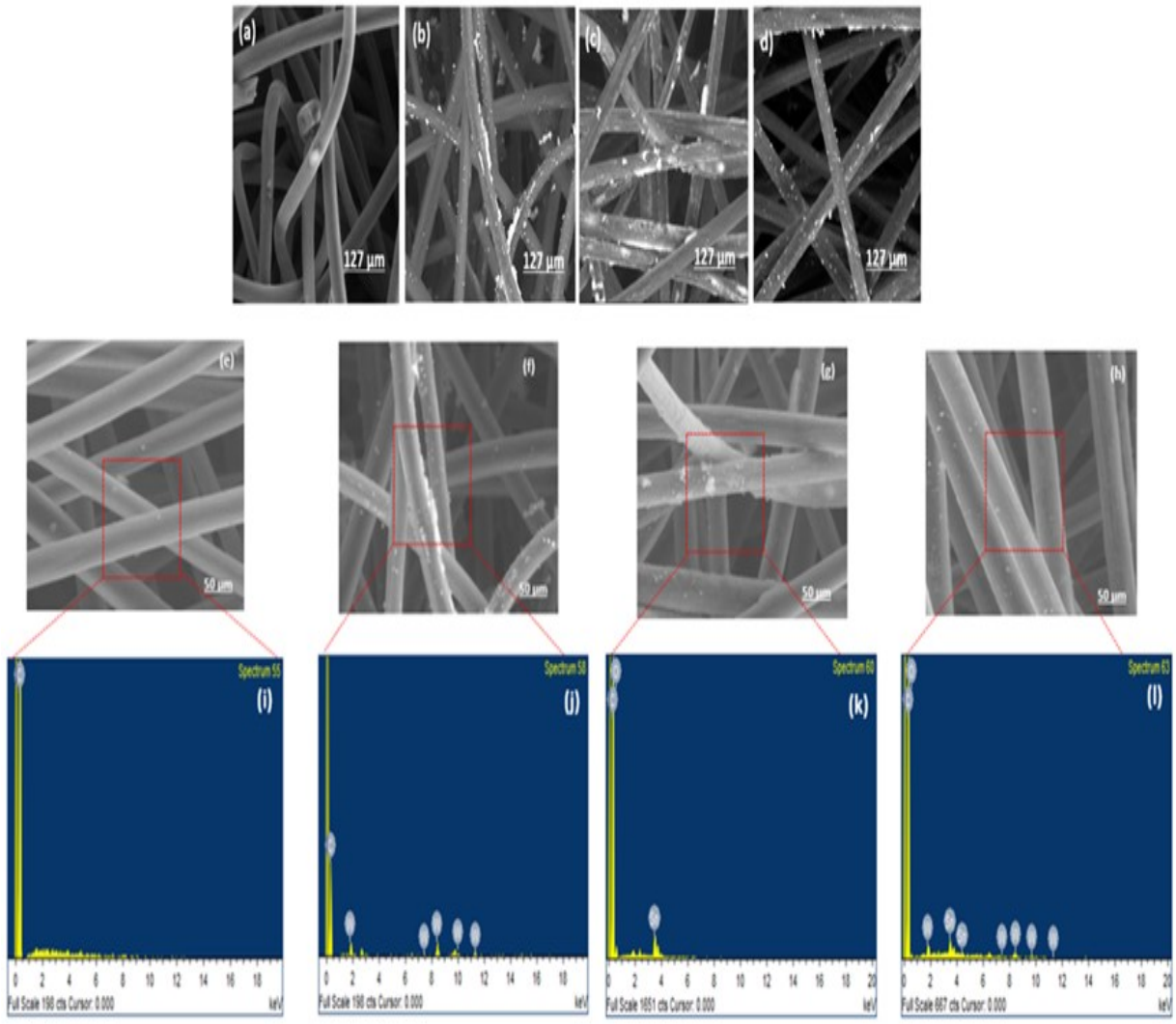

Figure 5.7: SEM images of different GF samples at magnification of 127 μm and 50 μm, respectively: (a and e) GF; (b and f) 0.07M W/GF; (c and g) 0.05M Sn/GF; (d and h) 0.025 M W-0.05M Sn/GF. (i) EDX analysis of the outlined area in image (e) of GF; (j) EDX analysis of the outlined area in image (f) of 0.07M W/GF; (k) EDX analysis of the outlined area in image (g) of 0.05M Sn/GF; (l) EDX analysis of the outlined area in image (h) of 0.025 M W-0.05M Sn/GF.

that some type of interaction between the two materials is occurring in order to enhance homogeneity of the solution.

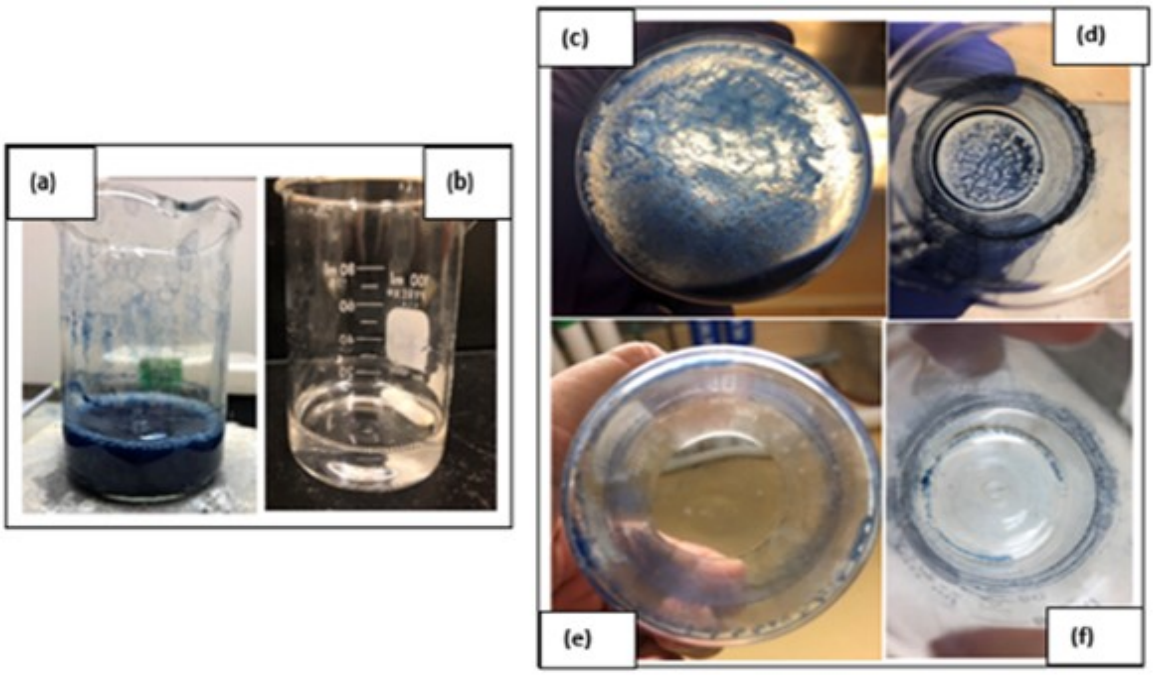

Figure 5.8: (a) Solution obtained after mixing 0.63 mmol WCl_6 and 0.013 mmol F-127 in 25 ml ethanol for 1 h at a room temperature. (b) Solution obtained after mixing 1.3 mmol $SnCl_4.5H_2O$ and 0.013 mmol F-127 in 25 ml ethanol for 1 h at room temperature. (c) and (d) Two different views of the remaining precipitate in the beaker shown in (a) after transferring the solution into an autoclave for solvothermal treatment. (e) and (f) The remaining precipitate after mixing both solutions in (a) and (b) after transferring the solution into an autoclave for solvothermal treatment.

To further investigate the elemental content of the modified GFs, energy dispersive X-ray spectroscopy (EDX) was used. Figure 5.7i presents the EDX spectrum of the area of as-received GF outlined in Figure 5.7e. Only C is detected by EDX in this sample. Figure 5.7j shows the EDX spectrum of the area of 0.07M W/GF highlighted in Figure 5.7f. The presence of C, O and W is detected in this sample with atomic percentages of 98.9%, 0.6% and 0.5%, respectively (Table 5.12). In the case of 0.05M Sn/GF, Figure 5.7k gives the EDX spectrum of the area highlighted in Figure 5.7g, which reveals the presence of C, O and Sn with atomic percentages of 87.6%, 11.4% and 1.0%, respectively. Lastly, Figure 5.7l shows the EDX spectrum obtained for the binary 0.025 M W-0.05M Sn/GF. As shown in Table 5.12, the atomic content of C, O, W and Sn in this sample is 94.8%, 4.9%, 0.1% and 0.2%, respectively. The atomic ratio of W:Sn here is 1:2 which is consistent with the molar ratio of W:Sn based on the amount mixed together to make the modified GF. Based on the images in Figure 5.8, it appears that all of the precursor for the mixed oxide was dissolved prior to autoclaving, indicating that all the W and Sn in the precursor was incorporated onto the GF surface. Hence, an atomic ratio of 1:2 for W:Sn is expected. These results indicate that this 1-step solvothermal method has successfully introduced O, W and Sn into the GF. Although EDX is much less accurate for quantitative analysis of the O content than the heavier W and Sn, it is interesting to note the much higher level of O when Sn is present than when W only is present. It is possible that this may play a role in the better oxide dispersion over the GF surface when modified by the mixture of oxides.

In order to characterize the chemical nature (i.e., oxidation state) and composition of the metal oxide components on the surfaces of the various GF samples, X-ray photoelectron

Table 5.12: The atomic content of C, O, W and Sn as obtained from Figures 5.7 (i, j, k and l) for various GFs samples.

Electrode/Element	**C**	**O**	**W**	**Sn**
	Atomic%			
GF (i)	100	-	-	-
0.07M W/GF (j)	98.89	0.57	0.54	-
0.05M Sn/GF (k)	87.55	11.42	-	1.03
0.025M W-0.05M Sn/GF (l)	94.76	4.88	0.13	0.24

spectroscopy (XPS) was conducted. As shown in the wide-range XPS survey spectrum of the various GF electrodes (Figure 5.9), the characteristic peaks of C, O, W and Sn are detected. As expected, the scan of the as-received GF surface displays only C and O peaks, while W and Sn peaks, in addition to C and O peaks, appear in the scans of 0.07M W/GF and 0.05M Sn/GF, respectively. In the case of 0.025M W-0.05 M Sn/GF, C, O, W and Sn peaks are observed. Overall, these results confirm the successful decoration of W and Sn on the GFs.

Figure 5.10 shows the narrow XPS spectra of C 1s obtained for the various modified GF samples with respect to as-received GF. The smaller C 1s peaks for the modified GF samples are in accord with previous studies indicating that the specific surface area and active sites on as-received GF surface have been enhanced due to the introduction of metal

oxide nanoparticles and oxygen functional groups, leading to improved electrochemical performance [54, 47, 101, 80]. This indicates that a sample with higher surface area exhibits a smaller and broader C 1s peak due to the growth in defective carbon content and the formation of carbon-oxygen bonds on the GF surface. For instance, Zhou *et al.* performed XPS analysis on ZrO_2-modified GF and reported the same trend for C 1s peaks. Zhou *et al.* found that the introduction of ZrO_2 on a GF surface led to an increase in defective carbon (C-sp^3) and decrease in graphitized carbon (C-sp^2) compared to that observed in unmodified GF and concluded that the formation of more defect sites contributes to enhancing the specific surface area, the number of active sites and GF hydrophilicity [54].

Figure 5.11 represents the narrow XPS spectra of O 1s for various GFs samples. As reported previously, the O 1s peaks for WO_3 and SnO_2 lattice are located at 530.6 eV and 530.9 eV, respectively [102, 94, 103, 104]. As evident from Figure 5.11, these peaks appear in the narrow scans of the modified GF samples. This supports the conclusion that the oxides that have formed are WO_3 and SnO_2. However, in addition to these peaks, a second peak/shoulder centred at $\sim$ 532.4 eV appears in the as-received and particularly both GF samples containing Sn. A peak at a more positive binding energy than that characteristic of SnO_2 indicates that this second form of oxygen is in a more oxidized form than that in SnO_2. It is possible that this second form of oxygen is associated with the additional oxygen content in the Sn-containing GF samples, as measured by EDX. The high-resolution scans in the W 4f XPS region (Figure 5.12) for the 0.07M W/GF and 0.025M W-0.05M Sn/GF samples show two discrete peaks centered at 35.60 eV and 37.97 eV for W $4f_{7/2}$ and W $4f_{5/2}$, respectively, with an energy separation of 4.37 eV and area ratio of $\sim$ 12.5:8.4, close to the theoretical ratio of 4:3. Based on the literature, these are the peaks expected

for W $4f_{7/2}$ and W $4f_{5/2}$ electrons when W is in the +6 oxidation state [105, 106, 68, 107]. This provides corroboratory evidence that WO_3 has formed. As shown in Figure 5.13, the high-resolution scans in the Sn 3d region for the 0.05M Sn/GF and 0.025 M W-0.05 M Sn/GF samples show peaks at 486.8 eV and 495.4 eV, which correspond to Sn $3d_{5/2}$ and Sn $3d_{3/2}$ electrons, respectively, and area ratio close to the theoretical ratio of 3:2. The energy separation between the observed Sn 3d peaks is 8.6 eV, indicating that Sn is in the +4 oxidation state [105, 67, 94, 107]. Again, this provides supporting evidence that SnO_2 has formed.

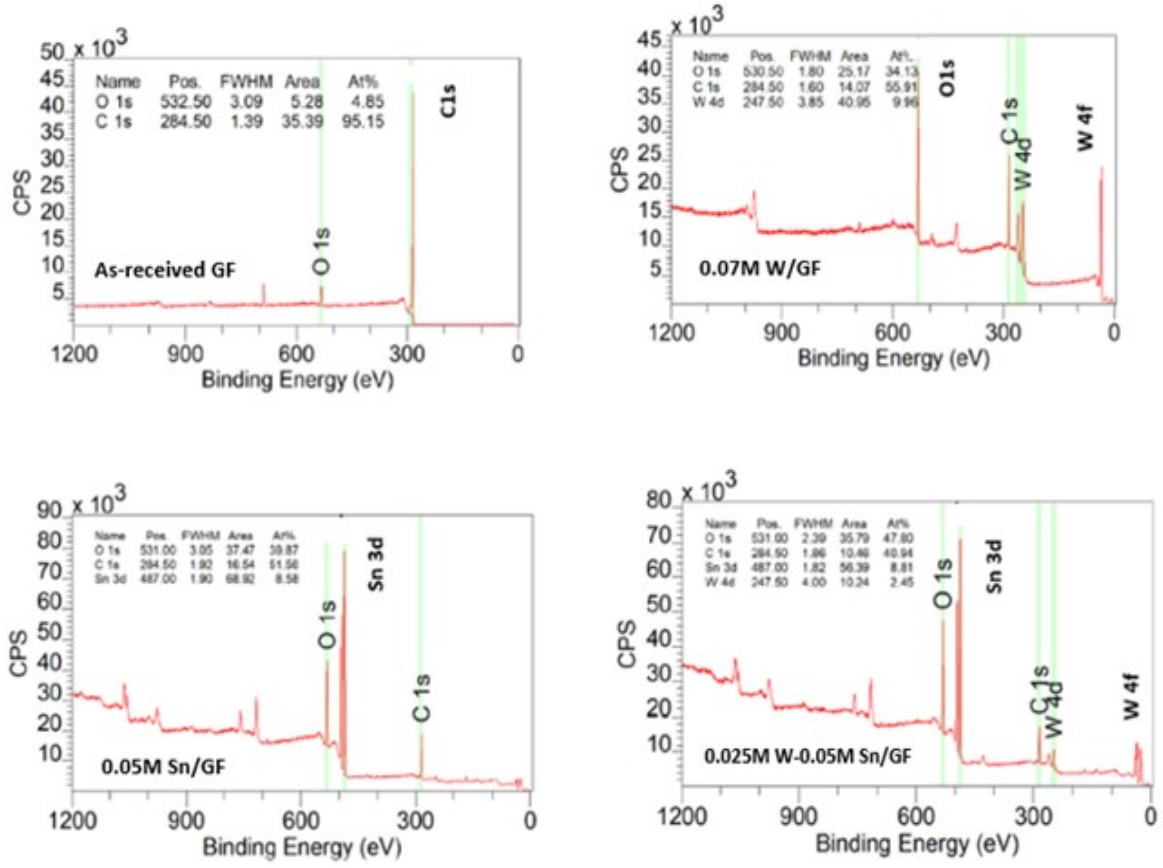

Figure 5.9: Wide-scan XPS survey spectrum of the various electrode materials (GF, 0.07M W/GF, 0.05M Sn/GF and 0.025 M W-0.05M Sn/GF).

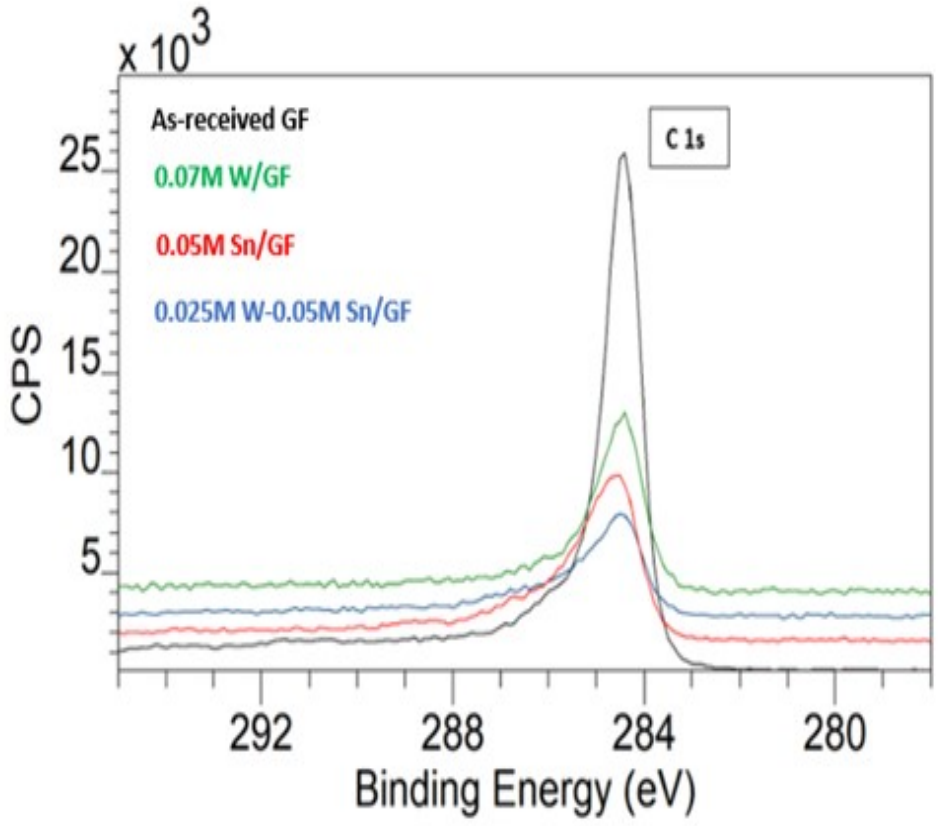

Figure 5.10: High-resolution XPS C 1s spectra of the different electrode materials (GF, 0.07M W/GF, 0.05M Sn/GF and 0.025 M W-0.05M Sn/GF).

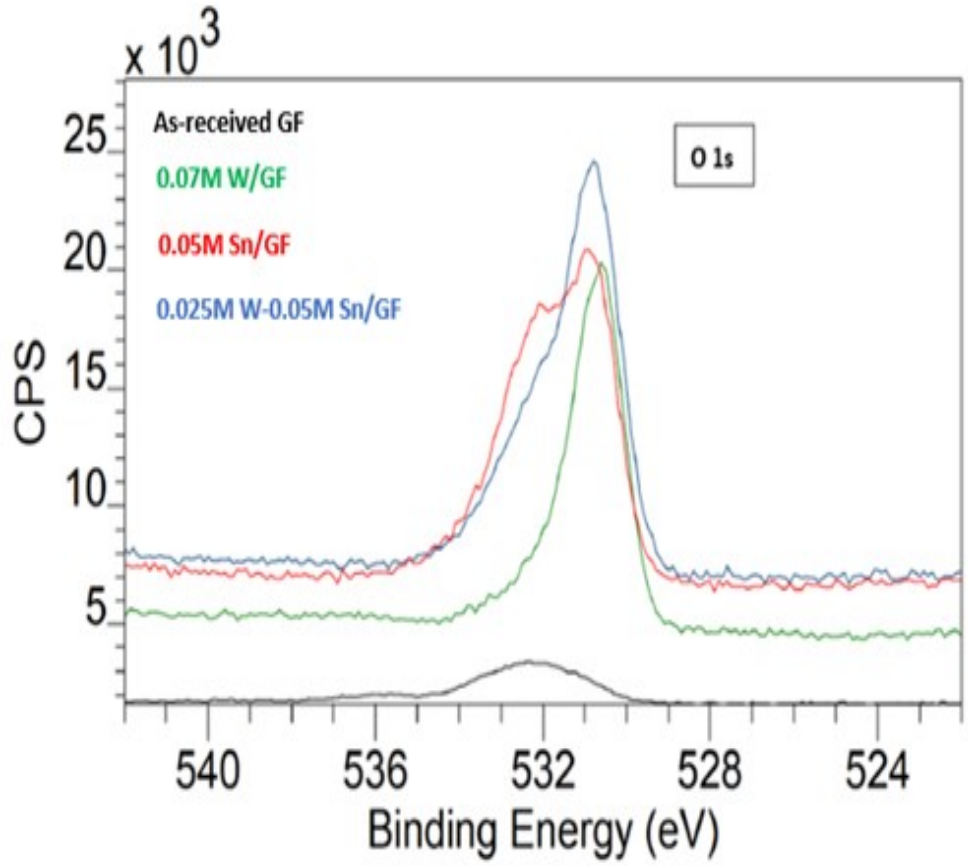

Figure 5.11: High-resolution XPS O1s spectra of the different electrode materials (GF, 0.07M W/GF, 0.05M Sn/GF and 0.025 M W-0.05M Sn/GF).

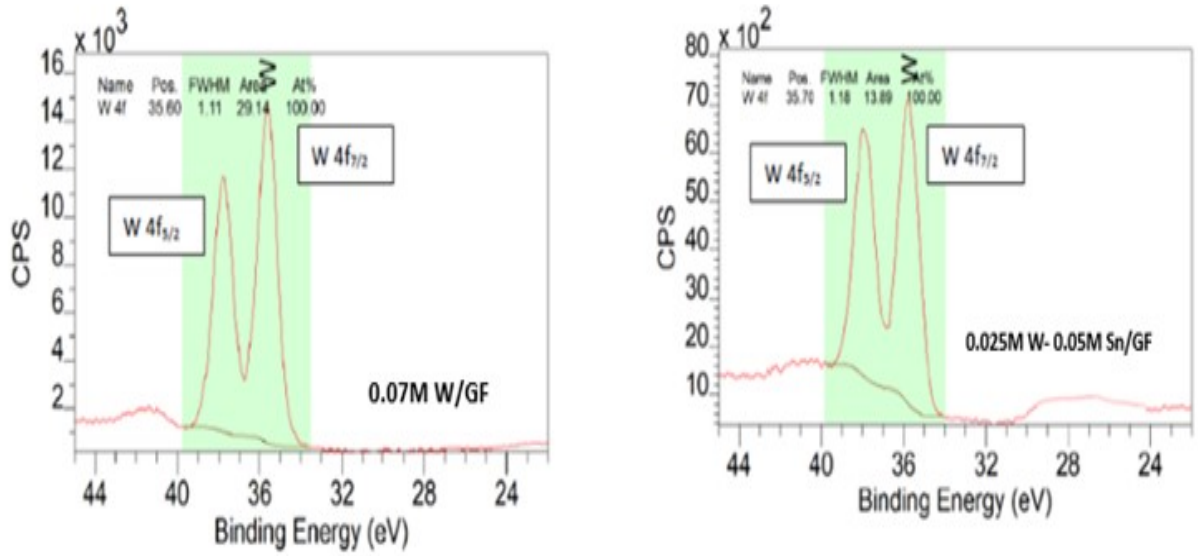

Figure 5.12: High-resolution XPS W 4f spectra of 0.07M W/GF and 0.025 M W-0.05M Sn/GF.

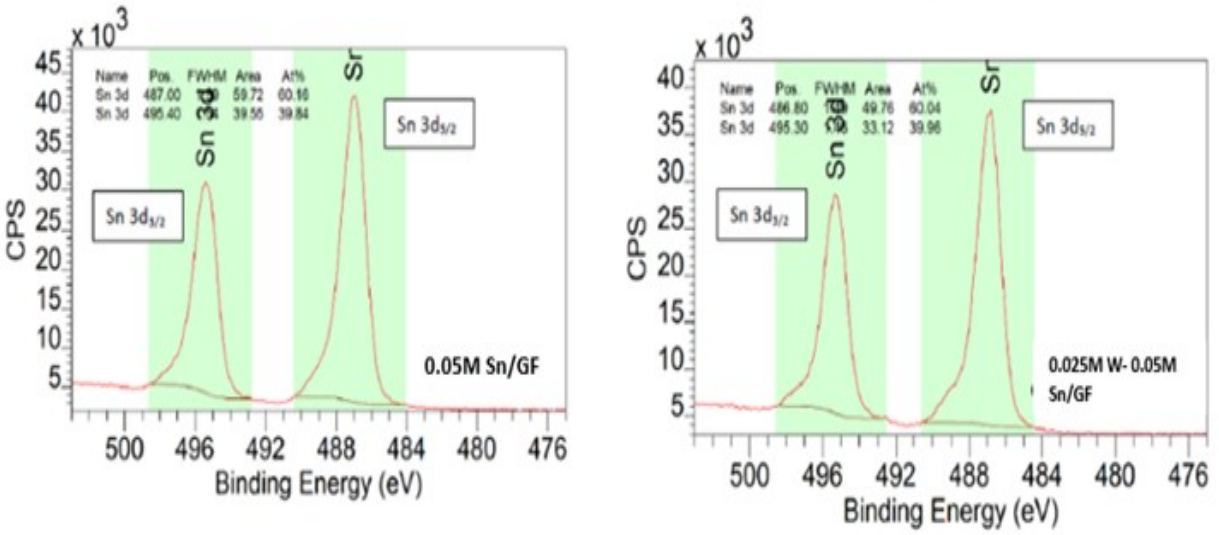

Figure 5.13: High-resolution XPS Sn 3d spectra obtained from 0.05M Sn/GF and 0.025M W-0.05M Sn/GF.

Chapter 6

SUMMARY AND RECOMMENDATIONS

6.1 Summary

The present thesis was designed to study the use of carbon-based materials as non-precious metal positive electrodes for hybrid Zn-Ce RFB. Graphite felts (GFs) have served as a promising carbon-based material to enhance the reversibility and kinetic activity for the Ce(III)/Ce(IV) system. However, GFs suffer from durability problems under the highly oxidizing conditions on the positive side of Zn-Ce RFB. Thus, decoration the GF with metal oxide nanoparticles was used in this study with the aim of improving GF electrochemical performance and mitigate its degradation problems. Tungsten trioxide (WO_3) and tin dioxide (SnO_2) using different precursor concentrations (i.e., 0.1M, 0.07M and 0.05M) were successfully introduced onto GF surface using a facile solvothermal method at 180

°C for 24 h. In addition, a novel binary metal oxide containing both WO_3 and SnO_2 at various compositions was successfully deposited onto GF surface using 1-step solvothermal approach at 180 °C for 24 h. It has been found that metal oxide modification improved the electrocatalytic performance of the unmodified GF toward the Ce(III)/Ce(IV) reaction significantly. Among all GF samples, the binary WO_3-SnO_2 modified GF exhibited the highest values of Q_a, Q_c and Q_c/Q_a. For example, Q_c/Q_a of as-received GF was found to improve from 17.8% to 50.1% when modified with 0.05M W and 0.05M Sn. Additionally, the binary 0.025M W-0.05 M Sn/GF electrode has demonstrated the most stable behavior and the lowest anodic and cathodic charge degradation rate of 39.3% and 29.4%, respectively, after 50 cycles compared to all tested electrodes. The improved results have been ascribed to the involvement of both metal oxides (WO_3 and SnO_2) in enhancing the electrochemical kinetics and the reversibility of Ce(III)/Ce(IV). SEM examination of the samples shows a more uniform distribution of finer oxide particles over the GF fibres when modified with a mixture of these oxides. Additionally, the introduction of oxygen functional groups has been achieved after the metal oxide decoration, contributing to better contact of electrolyte to the electrode surface and a lower energy barrier for the redox reaction at the electrolyte-electrode interface.

6.2 Recommendations for Future Work

The findings of this study are subjected to specific limitations. For instance, the graphite felt used in this study was obtained from only one vendor. Hence, it was not possible in this study to evaluate different graphite felts that have different properties from other vendors. Moreover, the electrochemical measurements were carried out only for a few op-

erating conditions including room temperature (23 °C), a specific electrolyte composition (0.05M Ce(III) MSA + 1.0M MSA) and unstirred conditions. The Ce(III) concentration used in this study is very low. Operation of an RFB at much higher concentrations is necessary to achieve the energy densities required for a viable RFB. Hence, a systematic experimental study in which these operating conditions are varied would be a fruitful area for further work. An issue that was not addressed in this study is the chemistry that occurs between the oxides involved in the binary modification. Thus, a deeper understanding of the reaction mechanism and the contribution of various catalysts in enhancing the kinetics of the Ce(III)/Ce(IV) reaction is crucial. Additionally, considerably more research is required to further improve the stability of binary metal oxide-modified GF electrodes in the strongly oxidizing environment of the positive electrolyte of Zn-Ce RFBs. Being limited to half-cell cyclic voltammetry experiments, this study lacks a more comprehensive evaluation of the modified GFs using other electrochemical measurements including galvanostatic charge/discharge, polarization curves and life-cycle analysis of full cells. Furthermore, the scope of this study was restricted to the utilization of graphite felts (GFs) as a positive electrode for the Zn-Ce RFB system. Further investigation and experimentation into other carbon-based materials (i.e., carbon felt (CF), carbon paper (CP), carbon plastic, glassy carbon, graphite powder, graphene and carbon nanotubes) could shed more light on the ways of improvement for such materials. Then, the most promising electrodes must be tested in an operating RFB. Finally, this work examined the decoration of GFs using a combination of WO_3 and SnO_2 as promising electrocatalysts. The study should be repeated using other single and binary metal oxides such as ZrO_2, Mn_2O_3, CeO_2, $NiCoO_2$, TiO_2 etc., in different combinations and dosing levels.

REFERENCES

[1] P. Leung, X. Li, C. Ponce De León, L. Berlouis, C. T. Low, and F. C. Walsh, "Progress in redox flow batteries, remaining challenges and their applications in energy storage," *RSC Adv.*, vol. 2, no. 27, pp. 10125–10156, 2012.

[2] K. Touati and F. Tadeo, *Pressure Retarded Osmosis as Renewable Energy Source*. Elsevier Inc., 2017.

[3] K. Azad, M. Rasul, M. Khan, and S. C. Sharma, *Introduction to sustainable and alternative ecofuels*. Elsevier Ltd., 2019.

[4] G. L. Soloveichik, "Flow Batteries: Current Status and Trends," *Chem. Rev.*, vol. 115, no. 20, pp. 11533–11558, 2015.

[5] W. S. Ebhota and T. C. Jen, "Fossil Fuels Environmental Challenges and the Role of Solar Photovoltaic Technology Advances in Fast Tracking Hybrid Renewable Energy System," *Int. J. Precis. Eng. Manuf. - Green Technol.*, vol. 7, no. 1, pp. 97–117, 2020.

[6] P. Alotto, M. Guarnieri, and F. Moro, "Redox flow batteries for the storage of renewable energy: A review," *Renew. Sustain. Energy Rev.*, vol. 29, pp. 325–335, 2014.

[7] J. Noack, N. Roznyatovskaya, T. Herr, and P. Fischer, "The Chemistry of Redox-Flow Batteries," *Angew. Chemie - Int. Ed.*, vol. 54, no. 34, pp. 9776–9809, 2015.

[8] K. J. Kim, M. S. Park, Y. J. Kim, J. H. Kim, S. X. Dou, and M. Skyllas-Kazacos, "A technology review of electrodes and reaction mechanisms in vanadium redox flow batteries," *J. Mater. Chem. A*, vol. 3, no. 33, pp. 16913–16933, 2015.

[9] J. Gostick and M. Pritzker, "Advanced Functional Materials Metal and Metal Oxide Electrocatalysts for Redox Flow Batteries," vol. 1910564, 2020.

[10] K. Amini and M. D. Pritzker, "Improvement of zinc-cerium redox flow batteries using mixed methanesulfonate-chloride negative electrolyte," *Appl. Energy*, vol. 255, no. September, p. 113894, 2019.

[11] M. H. Chakrabarti, S. A. Hajimolana, F. S. Mjalli, M. Saleem, and I. Mustafa, "Redox Flow Battery for Energy Storage," *Arab. J. Sci. Eng.*, vol. 38, no. 4, pp. 723–739, 2013.

[12] M. Uddin, M. F. Romlie, M. F. Abdullah, S. Abd Halim, A. H. Abu Bakar, and T. Chia Kwang, "A review on peak load shaving strategies," *Renew. Sustain. Energy Rev.*, vol. 82, no. February 2017, pp. 3323–3332, 2018.

[13] P. V. Kamat, K. S. Schanze, and J. M. Buriak, *Redox Flow Batteries*, vol. 2. 2017.

[14] G. Nikiforidis, R. Cartwright, D. Hodgson, D. Hall, and L. Berlouis, "Factors affecting the performance of the Zn-Ce redox flow battery," *Electrochim. Acta*, vol. 140, pp. 139–144, 2014.

[15] K. Amini and M. D. Pritzker, "Electrodeposition and electrodissolution of zinc in mixed methanesulfonate-based electrolytes," *Electrochim. Acta*, vol. 268, pp. 448–461, 2018.

[16] M. S.-K. Chris Menictas, Lim, and T. Mariana, *Advances in Batteries for Medium- and Large-scale Energy Storage*. Elsevier, 2014.

[17] F. Hussain, M. Z. Rahman, and A. Nair, *Chapter 6 - Energy storage technologies*. Elsevier Inc., 2020.

[18] C. Ponce de León, A. Frías-Ferrer, J. González-García, D. A. Szánto, and F. C. Walsh, "Redox flow cells for energy conversion," *J. Power Sources*, vol. 160, no. 1, pp. 716–732, 2006.

[19] X. Z. Yuan, C. Song, A. Platt, N. Zhao, H. Wang, H. Li, K. Fatih, and D. Jang, "A review of all-vanadium redox flow battery durability: Degradation mechanisms and mitigation strategies," *Int. J. Energy Res.*, vol. 43, no. 13, pp. 6599–6638, 2019.

[20] G. O. Mepsted and J. M. Moore, "Performance and durability of bipolar plate materials," *Handb. Fuel Cells*, pp. 1–8, 2010.

[21] F. Mezei, *Handbook of Batteries*. 2011.

[22] "Recent Advancements in All-Vanadium Redox Flow Batteries," *Advanced Materials Interfaces*, vol. 3, no. 1, pp. 1–22, 2016.

[23] J. H. Park, J. J. Park, O. O. Park, C. S. Jin, and J. H. Yang, "Highly accurate apparatus for electrochemical characterization of the felt electrodes used in redox flow batteries," *J. Power Sources*, vol. 310, pp. 137–144, 2016.

[24] P. K. Leung, M. R. Mohamed, A. A. Shah, Q. Xu, and M. B. Conde-Duran, "A mixed acid based vanadium-cerium redox flow battery with a zero-gap serpentine architecture," *J. Power Sources*, vol. 274, pp. 651–658, 2015.

[25] K. J. Kim, M. S. Park, Y. J. Kim, J. H. Kim, S. X. Dou, and M. Skyllas-Kazacos, "A technology review of electrodes and reaction mechanisms in vanadium redox flow batteries," *J. Mater. Chem. A*, vol. 3, no. 33, pp. 16913–16933, 2015.

[26] Z. Xie, Q. Liu, Z. Chang, and X. Zhang, "The developments and challenges of cerium half-cell in zinc-cerium redox flow battery for energy storage," *Electrochim. Acta*, vol. 90, pp. 695–704, 2013.

[27] R. Chen, S. Kim, and Z. Chang, "Redox Flow Batteries: Fundamentals and Applications," *Redox - Princ. Adv. Appl.*, 2017.

[28] P. K. Leung, C. Ponce-De-León, C. T. Low, A. A. Shah, and F. C. Walsh, "Characterization of a zinc-cerium flow battery," *J. Power Sources*, vol. 196, no. 11, pp. 5174–5185, 2011.

[29] Y. Li, P. Geysens, X. Zhang, J. Sniekers, J. Fransaer, K. Binnemans, and I. F. Vankelecom, "Cerium-containing complexes for low-cost, non-aqueous redox flow batteries (RFBs)," *J. Power Sources*, vol. 450, no. January, 2020.

[30] G. Nikiforidis, Y. Xiang, and W. A. Daoud, "Electrochemical behavior of carbon paper on cerium methanesulfonate electrolytes for zinc-cerium flow battery," *Electrochim. Acta*, vol. 157, pp. 274–281, 2015.

[31] G. Nikiforidis, "INVESTIGATIONS OF THE ZINC-CERIUM HYBRID FLOW BATTERY by," 2012.

[32] P. K. Leung, C. Ponce De León, C. T. Low, and F. C. Walsh, "Ce(III)/Ce(IV) in methanesulfonic acid as the positive half cell of a redox flow battery," *Electrochim. Acta*, vol. 56, no. 5, pp. 2145–2153, 2011.

[33] R. L. Clarke, S. H. B. J. Dougherty, S. Mohanta, and J. P. Millington, "Introducing Cerium Based High Energy Redox Batteries," pp. 1–6, 2002.

[34] "Review of zinc-based hybrid flow batteries: From fundamentals to applications," *Mater. Today Energy*, vol. 8, pp. 80–108, 2018.

[35] K. Amini and M. D. Pritzker, "Life-cycle analysis of zinc-cerium redox flow batteries," *Electrochimica Acta*, vol. 356, pp. 1–14, 2020.

[36] G. Nikiforidis, L. Berlouis, D. Hall, and D. Hodgson, "A study of different carbon composite materials for the negative half-cell reaction of the zinc cerium hybrid redox flow cell," *Electrochim. Acta*, vol. 113, pp. 412–423, 2013.

[37] F. C. Walsh, C. Poncedeléon, L. Berlouis, G. Nikiforidis, L. F. Arenas-Martínez, D. Hodgson, and D. Hall, "The development of Zn-Ce hybrid redox flow batteries for energy storage and their continuing challenges," *Chempluschem*, vol. 80, no. 2, pp. 288–311, 2015.

[38] P. K. Leung, C. Ponce-De-León, F. J. Recio, P. Herrasti, and F. C. Walsh, "Corrosion of the zinc negative electrode of zinc-cerium hybrid redox flow batteries in

methanesulfonic acid Batteries," *Journal of Applied Electrochemistry*, vol. 44, no. 9, pp. 1025–1035, 2014.

[39] R. Wang, Y. Li, and Y. L. He, "Achieving gradient-pore-oriented graphite felt for vanadium redox flow batteries: Meeting improved electrochemical activity and enhanced mass transport from nano- to micro-scale," *J. Mater. Chem. A*, vol. 7, no. 18, pp. 10962–10970, 2019.

[40] L. F. Arenas, C. Ponce De León, and F. C. Walsh, "Electrochemical redox processes involving soluble cerium species," *Electrochim. Acta*, vol. 205, no. March, pp. 226–247, 2016.

[41] K. A. Gschneidner, J. C. G. Bünzli, and V. K. Pecharsky, "Handbook on the Physics and Chemistry ofRare Earths," *Handbook on the Physics and Chemistry of Rare Earths*, vol. 36, 2006.

[42] L. F. Arenas, C. Ponce De León, and F. C. Walsh, "Electrochemical redox processes involving soluble cerium species," *Electrochimica Acta*, vol. 205, pp. 226–247, 2016.

[43] Z. Xie, D. Zhou, F. Xiong, S. Zhang, and K. Huang, "Cerium-zinc redox flow battery: Positive half-cell electrolyte studies," *J. Rare Earths*, vol. 29, no. 6, pp. 567–573, 2011.

[44] Z. Xie, F. Xiong, and D. Zhou, "Study of the Ce3+ /Ce4+ redox couple in mixed-acid media (CH3SO3H and H2SO4) for redox flow battery application," *Energy and Fuels*, vol. 25, no. 5, pp. 2399–2404, 2011.

[45] G. Nikiforidis, L. Berlouis, D. Hall, and D. Hodgson, "An electrochemical study on the positive electrode side of the zinc-cerium hybrid redox flow battery," *Electrochim. Acta*, vol. 115, pp. 621–629, 2014.

[46] M. H. Chakrabarti, N. P. Brandon, S. A. Hajimolana, F. Tariq, V. Yufit, M. A. Hashim, M. A. Hussain, C. T. Low, and P. V. Aravind, "Application of carbon materials in redox flow batteries," *J. Power Sources*, vol. 253, pp. 150–166, 2014.

[47] H. Zhang, N. Chen, C. Sun, and X. Luo, "Investigations on physicochemical properties and electrochemical performance of graphite felt and carbon felt for iron-chromium redox flow battery," *Int. J. Energy Res.*, no. December 2019, pp. 3839–3853, 2020.

[48] R. Smith, "Characterisation and Surface Modification of Graphitic Felts By Robert Smith," no. January, 2018.

[49] T. X. Huong Le, M. Bechelany, and M. Cretin, "Carbon felt based-electrodes for energy and environmental applications: A review," *Carbon N. Y.*, vol. 122, pp. 564–591, 2017.

[50] L. F. Castañeda, F. C. Walsh, J. L. Nava, and C. Ponce de León, "Graphite felt as a versatile electrode material: Properties, reaction environment, performance and applications," *Electrochim. Acta*, vol. 258, pp. 1115–1139, 2017.

[51] Y. Xiang and W. A. Daoud, "Cr2O3-modified graphite felt as a novel positive electrode for vanadium redox flow battery," *Electrochim. Acta*, vol. 290, pp. 176–184, 2018.

[52] W.-j. Lee, Y.-t. Wu, Y.-w. Liao, and Y.-t. Liu, "Graphite Felt Modified by Atomic Layer Deposition with TiO 2 Nanocoating Exhibits Super-Hydrophilicity , Low Charge-Transform Resistance , and High Electrochemical Activity," 2020.

[53] S. Zhong, C. Padeste, M. Kazacos, and M. Skyllas-Kazacos, "Comparison of the physical, chemical and electrochemical properties of rayon- and polyacrylonitrile-based graphite felt electrodes," *J. Power Sources*, vol. 45, no. 1, pp. 29–41, 1993.

[54] H. Zhou, Y. Shen, J. Xi, X. Qiu, and L. Chen, "ZrO2-Nanoparticle-Modified Graphite Felt: Bifunctional Effects on Vanadium Flow Batteries," *ACS Appl. Mater. Interfaces*, vol. 8, no. 24, pp. 15369–15378, 2016.

[55] R. Gautam, M. Kapoor, and A. Verma, "Batteries and Energy Storage Tactical surface modification of 3D graphite felt as electrode of vanadium redox flow batteries with enhanced electrolyte utilization and fast reaction kinetic," 2020.

[56] Y. Shen, H. Xu, P. Xu, X. Wu, Y. Dong, and L. Lu, "Electrochemical catalytic activity of tungsten trioxide- Modified graphite felt toward VO2+/VO2+ redox reaction," *Electrochim. Acta*, vol. 132, pp. 37–41, 2014.

[57] Z. He, Y. Jiang, W. Meng, F. Jiang, H. Zhou, Y. Li, J. Zhu, L. Wang, and L. Dai, "HF/H 2 O 2 treated graphite felt as the positive electrode for vanadium redox flow battery," *Appl. Surf. Sci.*, vol. 423, pp. 111–118, 2017.

[58] A. Di Blasi, O. Di Blasi, N. Briguglio, A. S. Aricò, D. Sebastián, M. J. Lázaro, G. Monforte, and V. Antonucci, "Investigation of several graphite-based electrodes for vanadium redox flow cell," *J. Power Sources*, vol. 227, pp. 15–23, 2013.

[59] B. Sun and M. Skyllas-Kazacos, "Modification of graphite electrode materials for vanadium redox flow battery application-I. Thermal treatment," *Electrochim. Acta*, vol. 37, no. 7, pp. 1253–1260, 1992.

[60] K. J. Kim, Y. J. Kim, J. H. Kim, and M. S. Park, "The effects of surface modification on carbon felt electrodes for use in vanadium redox flow batteries," *Materials Chemistry and Physics*, vol. 131, no. 1-2, pp. 547–553, 2011.

[61] T. X. H. Le, C. Charmette, M. Bechelany, and M. Cretin, "Facile Preparation of Porous Carbon Cathode to Eliminate Paracetamol in Aqueous Medium Using Electro-Fenton System," *Electrochimica Acta*, vol. 188, pp. 378–384, 2016.

[62] S. J. Yoon, "Development of modified graphite felt electrodes for the vanadium redox flow battery," 2020.

[63] G. Nikiforidis and W. A. Daoud, "Thermally Modified Graphite Electrodes for the Positive Side of the Zinc-Cerium Redox Flow Battery," *J. Electrochem. Soc.*, vol. 162, no. 6, pp. A809–A819, 2015.

[64] T. Hong, "Fundamental Study on Tin Recovery in Acidic Aqueous Systems," no. October, p. 139, 2015.

[65] A. Hassan and T. Tzedakis, "Enhancement of the electrochemical activity of a commercial graphite felt for vanadium redox flow battery (VRFB), by chemical treatment with acidic solution of K2Cr2O7," *J. Energy Storage*, vol. 26, no. July, p. 100967, 2019.

[66] C. Flox, M. Skoumal, J. Rubio-Garcia, T. Andreu, and J. R. Morante, "Strategies for enhancing electrochemical activity of carbon-based electrodes for all-vanadium redox flow batteries," *Appl. Energy*, vol. 109, pp. 344–351, 2013.

[67] Z. Na, X. Wang, D. Yin, and L. Wang, "Tin dioxide as a high-performance catalyst towards Ce(vi)/Ce(iii) redox reactions for redox flow battery applications," *J. Mater. Chem. A*, vol. 5, no. 10, pp. 5036–5043, 2017.

[68] Z. Na, X. Wang, D. Yin, and L. Wang, "Graphite felts modified by vertical two-dimensional WO3 nanowall arrays: High-performance electrode materials for cerium-based redox flow batteries," *Nanoscale*, vol. 10, no. 22, pp. 10705–10712, 2018.

[69] P. A. Shinde and S. C. Jun, "Review on Recent Progress in the Development of Tungsten Oxide Based Electrodes for Electrochemical Energy Storage," *ChemSusChem*, vol. 13, no. 1, pp. 11–38, 2020.

[70] X. Jiang, S. Lou, D. Chen, J. Shen, W. Han, X. Sun, J. Li, and L. Wang, "Fabrication of polyaniline/graphene oxide composite for graphite felt electrode modification and its performance in the bioelectrochemical system," *Journal of Electroanalytical Chemistry*, vol. 744, pp. 95–100, 2015.

[71] A. V. Kadam and S. B. Patil, "Polyaniline globules as a catalyst for WO3 nanoparticles for supercapacitor application," *Materials Research Express*, vol. 5, no. 8, 2018.

[72] J. W. Geng, Y. J. Ye, D. Guo, and X. X. Liu, "Concurrent electropolymerization of aniline and electrochemical deposition of tungsten oxide for supercapacitor," *J. Power Sources*, vol. 342, pp. 980–989, 2017.

[73] L. Wei, C. Xiong, H. R. Jiang, X. Z. Fan, and T. S. Zhao, "Highly catalytic hollow Ti3C2Tx MXene spheres decorated graphite felt electrode for vanadium redox flow batteries," *Energy Storage Mater.*, vol. 25, no. September 2019, pp. 885–892, 2020.

[74] Z. González, C. Flox, C. Blanco, M. Granda, J. R. Morante, R. Menéndez, and R. Santamaría, "Outstanding electrochemical performance of a graphene-modified graphite felt for vanadium redox flow battery application," *J. Power Sources*, vol. 338, pp. 155–162, 2017.

[75] D. M. Kabtamu, J. Y. Chen, Y. C. Chang, and C. H. Wang, "Electrocatalytic activity of Nb-doped hexagonal WO3 nanowire-modified graphite felt as a positive electrode for vanadium redox flow batteries," *J. Mater. Chem. A*, vol. 4, no. 29, pp. 11472–11480, 2016.

[76] K. B. Ibrahim, M. C. Tsai, S. A. Chala, M. K. Berihun, A. W. Kahsay, T. A. Berhe, W. N. Su, and B. J. Hwang, "A review of transition metal-based bifunctional oxygen electrocatalysts," *Journal of the Chinese Chemical Society*, vol. 66, no. 8, pp. 829–865, 2019.

[77] H. Zhou, J. Xi, Z. Li, Z. Zhang, L. Yu, L. Liu, X. Qiu, and L. Chen, "CeO2 decorated graphite felt as a high-performance electrode for vanadium redox flow batteries," *RSC Adv.*, vol. 4, no. 106, pp. 61912–61918, 2014.

[78] T. Liu, X. Li, H. Nie, C. Xu, and H. Zhang, "Investigation on the effect of catalyst on the electrochemical performance of carbon felt and graphite felt for vanadium flow batteries," *J. Power Sources*, vol. 286, pp. 73–81, 2015.

[79] R. K. Gautam and A. Verma, "Uniquely designed surface nanocracks for highly efficient and ultra-stable graphite felt electrode for vanadium redox flow battery," *Materials Chemistry and Physics*, vol. 251, no. May, p. 123178, 2020.

[80] Z. Na, X. Sun, and L. Wang, "Surface-functionalized graphite felts: Enhanced performance in cerium-based redox flow batteries," *Carbon N. Y.*, vol. 138, pp. 363–368, 2018.

[81] H. Osgood, S. V. Devaguptapu, H. Xu, J. Cho, and G. Wu, "Transition metal (Fe, Co, Ni, and Mn) oxides for oxygen reduction and evolution bifunctional catalysts in alkaline media," *Nano Today*, vol. 11, no. 5, pp. 601–625, 2016.

[82] K. B. Ibrahim, M. C. Tsai, S. A. Chala, M. K. Berihun, A. W. Kahsay, T. A. Berhe, W. N. Su, and B. J. Hwang, "A review of transition metal-based bifunctional oxygen electrocatalysts," *Journal of the Chinese Chemical Society*, vol. 66, no. 8, pp. 829–865, 2019.

[83] Z. Zhang, J. Liu, J. Gu, L. Su, and L. Cheng, "An overview of metal oxide materials as electrocatalysts and supports for polymer electrolyte fuel cells," *Energy and Environmental Science*, vol. 7, no. 8, pp. 2535–2558, 2014.

[84] C. M. Wu, S. Naseem, M. H. Chou, J. H. Wang, and Y. Q. Jian, "Recent advances in tungsten-oxide-based materials and their applications," *Front. Mater.*, vol. 6, no. March, pp. 1–17, 2019.

[85] Y. Xiang and W. A. Daoud, "Binary NiCoO2-modified graphite felt as an advanced positive electrode for vanadium redox flow batteries," *J. Mater. Chem. A*, vol. 7, no. 10, pp. 5589–5600, 2019.

[86] A. W. Bayeh, D. M. Kabtamu, Y. C. Chang, G. C. Chen, H. Y. Chen, T. R. Liu, T. H. Wondimu, K. C. Wang, and C. H. Wang, "Hydrogen-Treated Defect-Rich W18O49 Nanowire-Modified Graphite Felt as High-Performance Electrode for Vanadium Redox Flow Battery," *ACS Applied Energy Materials*, vol. 2, no. 4, pp. 2541–2551, 2019.

[87] L. Yu, F. Lin, W. Xiao, L. Xu, and J. Xi, "Achieving efficient and inexpensive vanadium flow battery by combining CexZr1xO2 electrocatalyst and hydrocarbon membrane," vol. 356, no. July 2018, pp. 622–631, 2019.

[88] B. Li, M. Gu, Z. Nie, Y. Shao, Q. Luo, X. Wei, X. Li, J. Xiao, C. Wang, V. Sprenkle, and W. Wang, "Bismuth nanoparticle decorating graphite felt as a high-performance electrode for an all-vanadium redox flow battery," *Nano Lett.*, vol. 13, no. 3, pp. 1330–1335, 2013.

[89] R. Wang, Y. Li, Y. Wang, and Z. Fang, "Phosphorus-doped graphite felt allowing stabilized electrochemical interface and hierarchical pore structure for redox flow battery," *Appl. Energy*, vol. 261, no. December 2019, p. 114369, 2020.

[90] A. W. Bayeh, D. M. Kabtamu, Y. C. Chang, G. C. Chen, H. Y. Chen, G. Y. Lin, T. R. Liu, T. H. Wondimu, K. C. Wang, and C. H. Wang, "Ta2O5-Nanoparticle-Modified Graphite Felt As a High-Performance Electrode for a Vanadium Redox Flow Battery," *ACS Sustainable Chemistry and Engineering*, vol. 6, no. 3, pp. 3019–3028, 2018.

[91] A. W. Bayeh, G.-y. Lin, Y.-c. Chang, D. M. Kabtamu, G.-c. Chen, H.-y. Chen, K.-c. Wang, Y.-m. Wang, T.-c. Chiang, H.-c. Huang, and C.-h. Wang, "Oxygen-Vacancy-

Rich Cubic CeO 2 Nanowires as Catalysts for Vanadium Redox Flow Batteries," 2020.

[92] X. Wen, D. Zhang, T. Yan, J. Zhang, and L. Shi, "Three-dimensional graphene-based hierarchically porous carbon composites prepared by a dual-template strategy for capacitive deionization," *Journal of Materials Chemistry A*, vol. 1, no. 39, pp. 12334–12344, 2013.

[93] Y. Sun, W. Wang, J. Qin, D. Zhao, B. Mao, Y. Xiao, and M. Cao, "Oxygen vacancy-rich mesoporous W18O49 nanobelts with ultrahigh initial Coulombic efficiency toward high-performance lithium storage," *Electrochim. Acta*, vol. 187, pp. 329–339, 2016.

[94] M. Yin, Y. Yao, H. Fan, and S. Liu, "WO3-SnO2 nanosheet composites: Hydrothermal synthesis and gas sensing mechanism," *Journal of Alloys and Compounds*, vol. 736, no. 2, pp. 322–331, 2018.

[95] L. Gao, F. Qu, and X. Wu, "Hierarchical WO3@SnO2 core-shell nanowire arrays on carbon cloth: A new class of anode for high-performance lithium-ion batteries," *Journal of Materials Chemistry A*, vol. 2, no. 20, pp. 7367–7372, 2014.

[96] PETER KGANYAGO, "WO 3 -SnO 2 nanostructures supported on carbon nanomaterials for electrochemical energy storage .," vol. 0002, no. August, 2017.

[97] Y. Zhang, L. Li, H. Su, W. Huang, and X. Dong, "Binary metal oxide: Advanced energy storage materials in supercapacitors," *J. Mater. Chem. A*, vol. 3, no. 1, pp. 43–59, 2015.

[98] L. Wei, J. Li, and X. Tang, "NOx storage at low temperature over MnOx-SnO 2 binary metal oxide prepared through different hydrothermal process," *Catal. Letters*, vol. 127, no. 1-2, pp. 107–112, 2009.

[99] Y. Yu, Y. Tan, H. Zhang, B. Yang, L. Yuan, X. Shen, and X. Hu, "Hybrid Sn–Co binary oxide nanosheets grown on carbon paper as the supercapacitor electrode materials," *J. Alloys Compd.*, vol. 814, p. 152199, 2020.

[100] P. Mazur, J. Mrlik, J. Pocedic, J. Vrana, J. Dundalek, J. Kosek, and T. Bystron, "Effect of graphite felt properties on the long-term durability of negative electrode in vanadium redox flow battery," *J. Power Sources*, vol. 414, no. January, pp. 354–365, 2019.

[101] S. Mehboob, G. Ali, H. J. Shin, J. Hwang, S. Abbas, K. Y. Chung, and H. Y. Ha, "Enhancing the performance of all-vanadium redox flow batteries by decorating carbon felt electrodes with SnO2 nanoparticles," *Applied Energy*, vol. 229, no. July, pp. 910–921, 2018.

[102] P. Charton, L. Gengembre, and P. Armand, "TeO2-WO3 glasses: Infrared, XPS and XANES structural characterizations," *Journal of Solid State Chemistry*, vol. 168, no. 1, pp. 175–183, 2002.

[103] M. Kwoka, L. Ottaviano, M. Passacantando, S. Santucci, G. Czempik, and J. Szuber, "XPS study of the surface chemistry of L-CVD SnO2 thin films after oxidation," *Thin Solid Films*, vol. 490, no. 1, pp. 36–42, 2005.

[104] J. Szuber, G. Czempik, R. Larciprete, D. Koziej, and B. Adamowicz, "XPS study of the L-CVD deposited SnO2 thin films exposed to oxygen and hydrogen," *Thin Solid Films*, vol. 391, no. 2, pp. 198–203, 2001.

[105] J. T. Kloprogge and B. J. Wood, *Handbook of Mineral Spectroscopy*. 2020.

[106] D. M. Kabtamu, J. Y. Chen, Y. C. Chang, and C. H. Wang, "Water-activated graphite felt as a high-performance electrode for vanadium redox flow batteries," *J. Power Sources*, vol. 341, pp. 270–279, 2017.

[107] C. D. Wagner, W. M. Riggs, L. E. Davis, J. F. Moulder, and G. E. Muilenberg, "Handbook of X-ray electron spectroscopy," 1992.